



1 **Subgrid Variations of the Cloud Water and Droplet Number**
2 **Concentration Over Tropical Ocean:**
3 **Satellite Observations and Implications for Warm Rain Simulation in**
4 **Climate Models**

5
6 Zhibo Zhang^{1,2*}, Hua Song², Po-Lun Ma³, Vincent E. Larson⁴, Minghuai Wang⁵, Xiquan Dong⁶,
7 Jianwu Wang⁷

- 8
9
10 1. Physics Department, University of Maryland Baltimore County (UMBC), Baltimore, MD,
11 USA
12 2. Joint Center for Earth Systems Technology, UMBC, Baltimore, MD, USA
13 3. Atmospheric Sciences and Global Change Division, Pacific Northwest National
14 Laboratory, Richland, WA, USA
15 4. Department of Mathematical Sciences, University of Wisconsin—Milwaukee, Milwaukee,
16 WI, USA
17 5. Institute for Climate and Global Change Research & School of Atmospheric Sciences,
18 Nanjing University, Nanjing, China
19 6. Department of Hydrology & Atmospheric Sciences, University of Arizona, Tucson, AZ,
20 USA
21 7. Department of Information System, UMBC, Baltimore, MD, USA

22
23 *Corresponding Author:
24 Dr. Zhibo Zhang
25 Email: Zhibo.Zhang@umbc.edu
26 Phone: +1 (410) 455 6315
27

28
29
30

31 **Abstract:**

32 One of the difficulties of simulating the warm rain process in global climate models (GCM)
33 is how to account for the impact of subgrid variations of cloud properties, such as cloud water
34 and cloud droplet number concentration, on the nonlinear precipitation processes such as
35 autoconversion. In practice, this impact is often treated by adding a so-called enhancement
36 factor term to the parameterization scheme. In this study, we derive the subgrid variations of
37 liquid-phase cloud properties over the tropical ocean using the satellite remote sensing products
38 from MODIS (Moderate Resolution Imaging Spectroradiometer) and investigate the
39 corresponding enhancement factors for the GCM parameterization of autoconversion rate. The
40 wide spatial coverage of the MODIS product enables us to depict a detailed quantitative picture
41 of the enhancement factor E_q due to the subgrid variation of cloud water, which shows a clear
42 cloud regime dependence, namely a significant increase from the stratocumulus (Sc) to cumulus
43 (Cu) cloud regions. Assuming a constant $E_q = 3.2$ would overestimate the observed E_q in the Sc
44 regions and underestimate it in the Cu regions. We also found that the E_q based on the
45 Lognormal PDF assumption performs slightly better than that based on the Gamma PDF
46 assumption. A simple parameterization scheme is provided to relate the E_q to the grid-mean
47 liquid cloud fraction, which can be readily used in GCMs. For the first time, the enhancement
48 factor E_N due to the subgrid variation of CDNC is derived from satellite observation, and results
49 reveal several regions downwind of biomass burning aerosols (e.g., Gulf of Guinea, East Coast of
50 South Africa), air pollution (i.e., Eastern China Sea), and active volcanos (e.g., Kilauea Hawaii and
51 Ambae Vanuatu), where the E_N is comparable, or even larger than E_q , even after the optically
52 thin clouds are screened out.

53

54



55 1. Introduction

56 Clouds are a strong modulator of Earth's radiative energy budget (Klein and Hartmann,
57 1993; Trenberth et al., 2009). They can interact with other components of the climate system,
58 such as ocean, land, and aerosols, in various ways. The feedback of clouds to climate change
59 remains one of the largest uncertainties in our understanding of the climate sensitivity (Bony and
60 Dufresne, 2005; Soden and Held, 2006). Despite their importance in the climate system,
61 simulating clouds in conventional general circulations models (GCM) has proved to be extremely
62 challenging. A main difficulty is rooted in the fact the typical grid size of GCM (~100km) is much
63 larger than the spatial scale of many cloud microphysical processes, and as a result these subgrid
64 scale processes, as well as the subgrid cloud variations, have to be highly simplified and then
65 parameterized as functions of resolved, grid-level variables.

66 Of particular interest in this study is the warm rain processes in liquid-phase clouds, which
67 have fundamental impacts on the cloud water budget and lifetime. Although in reality it is highly
68 complicated and involves multiple factors, warm rain formation in GCMs is usually parameterized
69 as simple functions of only key cloud parameters. For example, the drizzle in MBL cloud is
70 initialized by the so-called autoconversion process in which the collision-coalescence of cloud
71 droplets gives birth to large drizzle drops (Pruppacher and Klett, 1997). In GCMs, for the sake of
72 efficiency, this process is usually parameterized as a function of liquid water content (LWC or
73 symbol q_c) and cloud droplet number concentration (CDNC or symbol N_c) (Khairoutdinov and
74 Kogan, 2000) (see section 2 for details). Even though this is highly simplified, the parametrization
75 scheme still faces a great difficulty. The calculation of grid-mean autoconversion efficiency
76 requires the knowledge of subgrid distributions of LWC and CDNC, but in the GCMs only grid-
77 mean quantities $\langle q_c \rangle$ and $\langle N_c \rangle$ are known and available for use in the computation of
78 autoconversion rate. As pointed out by Pincus and Klein (2000), for a process $f(x)$ such as
79 autoconversion that is nonlinearly dependent on subgrid variables, x , the grid-mean value $\langle f(x) \rangle$
80 is not equal to the value estimated based on the grid-mean $\langle x \rangle$, i.e., $\langle f(x) \rangle \neq f(\langle x \rangle)$.
81 Mathematically, if $f(x)$ is convex, then $f(\langle x \rangle) < \langle f(x) \rangle$ (Larson and Griffin, 2013; Larson et al.,
82 2001). To take this effect into account, a parameter E is often introduced in the GCM as part of
83 the parameterization such that $\langle f(x) \rangle = E \cdot f(\langle x \rangle)$. It is referred to as the "enhancement factor"



84 in many studies and this study too because $E > 1$ for a convex function. Such a nonlinear effect
85 is not just limited to the autoconversion process. Some other examples are the plane-parallel
86 albedo bias (Barker, 1996; Cahalan et al., 1994; Oreopoulos and Davies, 1998a), subgrid cloud
87 droplet activation (Morales and Nenes, 2010) and accretion (Boutle and Abel, 2012; Lebsock et
88 al., 2013).

89 The value of E is determined primarily by two factors: the nonlinearity of $f(x)$ and the
90 subgrid probability density function (PDF) $P(x)$. Given the same subgrid variation of LWC, i.e.,
91 $P(q_c)$, the nonlinear effect impacts the autoconversion process more than it does on the
92 accretion process, because the former is a more nonlinear function of q_c than the latter. For the
93 same $f(x)$, a grid box with a narrow and symmetric $P(x)$ would require a smaller E than another
94 grid box with a broader and non-symmetric $P(x)$. The shape of the $P(x)$ is dependent on mainly
95 on cloud regime. Take cloud water for example. The subgrid PDF of cloud water $P(q_c)$ is usually
96 narrower and more Gaussian-like in the stratocumulus (Sc) region while in the broken cumulus
97 (Cu) cloud region, $P(q_c)$ is usually broader and more skewed (Barker et al., 1996; Lee et al., 2010;
98 Oreopoulos and Cahalan, 2005; Wood and Hartmann, 2006). Obviously, model resolution is also
99 an important factor—the coarser the spatial resolution, the larger the subgrid cloud
100 inhomogeneity. Ideally, the value of the enhancement factor E should be diagnosed from the
101 subgrid cloud PDF $P(x)$, which should be scale aware and dependent on cloud regime.
102 Unfortunately, because this is not possible in most conventional GCMs, the value of E is usually
103 assumed to be a constant for the lack of better options. The E for autoconversion due to subgrid
104 LWC variation is assumed to be 3.2 in the two-moment cloud microphysics parameterization
105 schemes by Morrison and Gettelman (2008) (MG scheme hereafter), which is employed in the
106 widely used Community Atmosphere Model (CAM). This choice of $E = 3.2$ is based on an early
107 study by Barker et al. (1996), in which the mesoscale variation of column-integrated optical
108 thickness of the “overcast stratocumulus”, “broken stratocumulus” and “scattered
109 stratocumulus” are studied. The value $E = 3.2$ is derived based on the mesoscale variation of the
110 broken stratocumulus.

111 Clearly, a simple constant E is not adequate. The following is a list of attempts to better
112 understand the subgrid cloud variations and the implications for warm rain simulations in GCMs.



113 Several previous studies have shown that the mesoscale cloud water variation is a strong function
114 of cloud regime—the subgrid cloud water variation of Sc cloud is much different from that of Cu
115 clouds (Barker et al., 1996; Lee et al., 2010; Oreopoulos and Cahalan, 2005; Wood and Hartmann,
116 2006). As the first part of a two-part study, Larson and Griffin (2013) first laid out a systematic
117 theoretical basis for understanding the effects of subgrid cloud property variations on simulating
118 various nonlinear processes in GCM, including not only the autoconversion but also the accretion,
119 condensation, evaporation and sedimentation processes. In the second part, using cloud fields
120 from a large-eddy simulation (LES), Griffin and Larson (2013) showed that inclusion of the
121 enhancement factor indeed leads to more rainwater at surface in single-column simulations and
122 makes them agree better with high-resolution large-eddy simulations. Using a combination of in
123 situ measurement and satellite remote sensing data, Boutle et al. (2014) analyzed the spatial
124 variation of cloud and rain water, as well as their covariation. They further developed a simple
125 parameterization scheme to relate the subgrid cloud water variance to the grid-mean cloud
126 fraction. Recently, using the ground-based observations from three Department of Energy (DOE)
127 Atmospheric Radiation Measurement (ARM) sites, Xie and Zhang (2015) developed a scale-aware
128 parameterization scheme for GCMs to account for subgrid cloud water variation. Although these
129 previous studies have shed important light on subgrid cloud variation and the implications for
130 GCM, they lack a global perspective because they are only based on limited data (e.g., LES cases,
131 in situ and ground-based measurement). Currently, satellite remote sensing observation is the
132 only way to achieve a global perspective, although remote sensing products suffer from inherent
133 retrieval uncertainties. Using the observations from the space-borne radar CloudSat, Lebsock et
134 al. (2013) showed that the subgrid cloud water variance is larger over the Sc region than over the
135 Cu region, and as a result the enhancement factor shows an increasing trend from Sc to Cu region.
136 They also highlighted importance of considering the subgrid co-variability of cloud water and rain
137 water in the computation of the accretion rate. On the modeling side, Guo et al. (2014)
138 investigated the sensitivity of cloud simulation in the Geophysical Fluid Dynamics Laboratory
139 (GFDL) Atmospheric General Circulation Model (AM) to the subgrid cloud water parameterization
140 schemes. A similar study was carried out by Bogenschutz et al. (2013) using the National Center
141 of Atmospheric Research (NCAR) Community Atmospheric Model (CAM). Both studies show that



142 the more sophisticated subgrid parameterization scheme— Cloud Layers Unified by Binormals
143 (CLUBB) (Golaz et al., 2002a; 2002b; Larson et al., 2002)—lead to a better simulation of clouds in
144 the model. However, a more recent study by Song et al. (2017) reveals that the CLUBB in CAM
145 version 5.3 (CAM5.3) overestimates the enhancement factor in the trade wind cumulus cloud
146 region, which in turn leads to the “empty cloud” problem.

147 Despite these previous studies, many questions remain unanswered. First of all, all the
148 previous studies, as far as we know, have focused on the impact of subgrid cloud water variation.
149 The potential impact of subgrid variation of cloud microphysics, namely CDNC, has been
150 overlooked so far. Given the same amount of cloud water, a cloud with a smaller CDNC would
151 have larger droplets and therefore larger precipitation efficiency than another cloud with a larger
152 CDNC. Secondly, most of previous studies are based on the assumption that the subgrid cloud
153 property variation follows certain well-behaved distributions, usually either Gamma (e.g., Barker,
154 1996; Morrison and Gettelman, 2008; Oreopoulos and Barker, 1999; Oreopoulos and Cahalan,
155 2005) or Lognormal (Boutle et al., 2014; Larson and Griffin, 2013; e.g., Lebsock et al., 2013).
156 However, the validity and performance of the assumed PDF shape are seldom checked.
157 Furthermore, although the study by Lebsock et al. (2013) has depicted a global picture of the
158 enhancement factor for the autoconversion modeling in GCM, the picture is far from clear due
159 to the small sampling rate of CloudSat observations.

160 In this study, we revisit the subgrid variations of liquid-phase cloud properties over the
161 tropical ocean using 10 years of MODIS cloud observations, with the overarching goal to better
162 understand the potential impacts of subgrid cloud variations on the warm rain processes in the
163 conventional GCMs. Similar to previous studies, we will quantify the subgrid cloud water
164 variations based on MODIS observations. Going one step further, we will also attempt to unveil
165 for the first time the subgrid CDNC variation and investigate its implications for warm rain
166 simulations in GCM. Moreover, we will take advantage of the wide spatial coverage of MODIS
167 data to achieve a more detailed picture of the enhancement factor for the autoconversion
168 simulation. Last but not least, we will evaluate the two widely used distributions, i.e., Lognormal



169 and Gamma, in terms of their performance and limitations for simulating the enhancement
170 factor.

171 The rest of the paper is organized as follows, we will first explain the theoretical
172 background in Section 2 and introduce the data and methodology in Section 3. The MODIS
173 observations of the grid mean values and subgrid variations of key cloud properties will be
174 presented and discussed in Section 4. The implications for the autoconversion process simulation
175 in the GCMs will be discussed in 5. The main findings will be summarized in Section 6 with an
176 outlook for future studies.

177 2. Theoretical Background

178 2.1. Theoretical Distributions to describe subgrid cloud property variations

179 In previous studies, the spatial variations of cloud properties, such as cloud optical thickness
180 (COT), cloud liquid water path (LWP) and cloud liquid water content (LWC), are often described
181 using either of two theoretical distributions—the Gamma and Lognormal distribution. The
182 probability density function (PDF) from a Gamma distribution is a two-parameter function as
183 follows (Barker, 1996; Oreopoulos and Davies, 1998b):

$$P_G(x) = \frac{1}{\Gamma(v)} \alpha^v x^{v-1} \exp(-\alpha x), \quad (1)$$

184 where Γ is the Gamma function, v is the so-called inverse relative variance, and α the so-called
185 rate parameter. The mean value of a Gamma distribution is given by

$$\langle x \rangle = \int_0^\infty x P_G(x) dx = \frac{v}{\alpha}, \quad (2)$$

186 and the variance given by

$$Var(x) = \int_0^\infty (x - \langle x \rangle)^2 P_G(x) dx = \frac{v}{\alpha^2}. \quad (3)$$

187 It follows from Eq. (2) and (3) that the inverse relative variance

$$v = \frac{1}{\eta} = \frac{\langle x \rangle^2}{Var(x)}, \quad (4)$$

188 where $\eta = \frac{Var(x)}{\langle x \rangle^2}$ is the relative variance.



189 The PDF of a Lognormal distribution is given as follows (Larson and Griffin, 2013;
 190 Lebsack et al., 2013):

$$P_L(x) = \frac{1}{\sqrt{2\pi}x\sigma} \exp\left(-\frac{(\ln x - \mu)^2}{2\sigma^2}\right), \quad (5)$$

191 where $\mu = \langle \ln x \rangle$ and $\sigma^2 = \text{Var}(\ln x)$ are the two parameters that determine the shape of the
 192 Lognormal distribution and correspond to the mean and variance of $\ln x$, respectively. The
 193 mean value of the Lognormal distribution is given by

$$\langle x \rangle = \int_0^\infty x P_L(x) dx = e^{\mu + \frac{\sigma^2}{2}}, \quad (6)$$

194 and the variance given by

$$\text{Var}(x) = \int_0^\infty (x - \langle x \rangle)^2 P_L(x) dx = e^{2\mu + \sigma^2} (e^{\sigma^2} - 1). \quad (7)$$

195 It follows from Eq. (6) and (7) that the inverse relative variance can be derived from the
 196 following equation

$$e^{\sigma^2} = 1 + \frac{\text{Var}(x)}{\langle x \rangle^2} = 1 + \frac{1}{v}. \quad (8)$$

197 An example of the Gamma and Lognormal distributions for LWC is shown in Figure 1a. In this
 198 example, both distributions have the same mean $\langle LWC \rangle = 0.5 \text{ g/kg}$ and also the same inverse
 199 relative variance $v = 3$. Although the general shapes of the two PDFs are similar, they differ
 200 significantly at the two ends: the Gamma PDF is larger than Lognormal PDF over the small values
 201 of LWC, and the opposite is true over the large values of LWC. The Gamma and Lognormal
 202 distributions can also be used to describe the spatial variation of CDNC (Gultepe and Isaac, 2004).
 203 An example is given in Figure 1c, in which the $LWC = 0.5 \text{ g/kg}$, the mean CDNC $\langle N_c \rangle = 50 \text{ cm}^{-3}$,
 204 and the inverse relative variance of CDNC $v = 5.0$.

205 Both Gamma and Lognormal distributions are mathematically convenient. For example,
 206 if any physical process $M(x)$ is a power function of x ,

$$M(x) = Kx^\beta, \quad (9)$$

207 then if x follows the Gamma distribution, the expected value $\langle M(x) \rangle$ is given by

$$\langle M(x) \rangle_G = K \int_0^\infty x^\beta P_G(x) dx = \frac{\Gamma(v+\beta)}{\Gamma(v)v^\beta} K \langle x \rangle^\beta, \quad \beta > -v. \quad (10)$$

208 Similarly if x follows the Lognormal distribution, the expected value of $\langle M(x) \rangle$ is



$$\langle M(x) \rangle_L = K \int_0^{\infty} x^{\beta} P_L(x) dx = (e^{\sigma^2})^{\frac{\beta^2 - \beta}{2}} K \langle x \rangle^{\beta}. \quad (11)$$

209 Thus, the expected value of $\langle M(x) \rangle$ can be computed from the analytical solutions above,
 210 instead of a numerical integration over the PDF. However, it is important to note that Eq. (10) is
 211 only valid when $\beta > -v$. The Gamma function $\Gamma(v + \beta)$ can run into singular values when $v +$
 212 $\beta < 0$. In contrast, Eq. (11) is valid for any real value β . This is one advantage of the Lognormal
 213 distribution over the Gamma distribution.

214 2.2. Impacts of subgrid cloud variations on warm rain simulations in climate models

215 As pointed out in Pincus and Klein (2000), the subgrid cloud property variations have
 216 important implications for modeling the nonlinear cloud processes in climate models, such as the
 217 precipitation and radiative transfer processes. Of particular interest to this study is the auto-
 218 conversion process that initializes the warm rain in marine boundary layer clouds. Following
 219 Khairoutdinov and Kogan (2000) (“KK2000” hereafter), the auto-conversion rate is often modeled
 220 in GCMs as a power function of LWC and cloud droplet number concentration (CDNC) as follows

$$\frac{\partial q_r}{\partial t} = C (q_c)^{\beta_q} (N_c)^{\beta_N}, \quad (12)$$

221 where $\frac{\partial q_r}{\partial t}$ is the rain water tendency due to the auto-conversion process, q_c is the cloud water
 222 mixing ratio in the unit of kg/kg, N_c is the CDNC in the unit of cm^{-3} . The three parameters $C =$
 223 1350, $\beta_q = 2.47$ and $\beta_N = -1.79$ are derived through a least-square fitting of the rain rate
 224 results from a large-eddy simulation. The KK2000 scheme has been adopted in the popular two-
 225 moment cloud microphysics scheme for GCMs developed by Morrison and Gettelman (2008)
 226 (referred to as MG scheme). Ideally, if the subgrid variations of q_c and N_c are known, then the
 227 grid-mean in-cloud auto-conversion rate can be derived from the following integral

$$\left\langle \frac{\partial q_r}{\partial t} \right\rangle = \int_0^{\infty} \int_0^{\infty} C (q_c)^{\beta_q} (N_c)^{\beta_N} P(q_c, N_c) dq_c dN_c, \quad (13)$$

228 where $P(q_c, N_c)$ is the joint PDF of q_c and N_c . Unfortunately, most conventional GCMs lack the
 229 capability of predicting the subgrid variations of cloud properties, with only a couple of
 230 exceptions (Thayer-Calder et al., 2015). What is known from the GCM is usually the in-cloud
 231 grid-mean values $\langle q_c \rangle$ and $\langle N_c \rangle$. As a result, instead of using Eq. (13), the auto-conversion rate
 232 in GCMs is usually computed from the following equation



$$\left\langle \frac{\partial q_r}{\partial t} \right\rangle = E \cdot C(\langle q_c \rangle)^{\beta_q} (\langle N_c \rangle)^{\beta_N}, \quad (14)$$

233 where E is referred to as the “enhancement factor” in Morrison and Gettelman (2008), or the

234 “subgrid scale homogeneity bias” in Pincus and Klein (2000). By definition its value is the ratio

$$E = \frac{\int_0^\infty \int_0^\infty (q_c)^{\beta_q} (N_c)^{\beta_N} P(q_c, N_c) dq_c dN_c}{(\langle q_c \rangle)^{\beta_q} (\langle N_c \rangle)^{\beta_N}}. \quad (15)$$

235 The root of this enhancement factor is that the auto-conversion process is a non-linear function

236 of q_c and N_c . As a result, the rain rate computed based on the grid-mean values $\langle q_c \rangle$ and $\langle N_c \rangle$

237 would be biased in comparison with the result from the integral in Eq. (13) (Pincus and Klein,

238 2000). Obviously, the value of the enhancement factor depends on the subgrid variations of q_c

239 and N_c . If clouds are homogenous on the subgrid scale, then $E \sim 1$. The more inhomogeneous

240 the clouds are, the larger the E is. In the special case where q_c and N_c are independent, then the

241 joint PDF $P(q_c, N_c)$ becomes $P(q_c, N_c) = P(q_c)P(N_c)$, where $P(q_c)$ and $P(N_c)$ are the PDF of

242 the subgrid q_c and N_c . Consequently, Eq. (13) reduces to

$$\left\langle \frac{\partial q_r}{\partial t} \right\rangle = C \int_0^\infty (q_c)^{\beta_q} P(q_c) dq_c \int_0^\infty (N_c)^{\beta_N} P(N_c) dN_c. \quad (16)$$

243 And Eq.(15) reduces to

$$E = E_q \cdot E_N, \quad (17)$$

244 where E_q is the enhancement factor due to the subgrid variation of cloud water which has the

245 form,

$$E_q = \frac{\int_0^\infty \int_0^\infty (q_c)^{\beta_q} P(q_c) dq_c}{(\langle q_c \rangle)^{\beta_q}}, \quad (18)$$

246 and the E_N is the enhancement factor due to the subgrid variation of cloud water which has the

247 form,

$$E_N = \frac{\int_0^\infty \int_0^\infty (N_c)^{\beta_N} P(N_c) dN_c}{(\langle N_c \rangle)^{\beta_N}}. \quad (19)$$

248



249 Because most current GCMs do not have the capability to simulate the subgrid cloud
 250 property variations, models usually use pre-defined subgrid cloud variations in the computation
 251 of grid-mean auto-conversion rate instead of using prognostic values. For example, in the MG
 252 scheme for the CAM5.3, the subgrid LWC is assumed to follow the Gamma distribution in Eq. (1).
 253 Furthermore, it is assumed that the subgrid variation of CDNC is small and therefore the
 254 enhancement factor due to CDNC variation is negligible (i.e., close to unity). Substituting the
 255 Gamma distribution in Eq. (1) into the definition equation of enhancement factor in Eq.(18), and
 256 with help from Eq. (10), one can derive that

$$E(P_G, \beta) = \frac{1}{\langle x \rangle^\beta} \int_0^\infty x^\beta P_G(x) dx = \frac{\Gamma(v+\beta)}{\Gamma(v)v^\beta}, \quad (20)$$

257 where $x \sim q_c$, $\beta = \beta_q = 2.47$ for the enhancement factor for the KK2000 scheme due to the
 258 subgrid variation of cloud water. In addition to the Gamma distribution, some studies also use
 259 the Lognormal distribution to account for the subgrid cloud water variation (Lebsock et al., 2013).
 260 In such case, substituting the Lognormal distribution in Eq. (5) into Eq.(18), and with help from
 261 Eq.(11), one can find that the enhancement factor for the Lognormal distribution is given by

$$E(P_L, \beta) = \frac{1}{\langle x \rangle^\beta} \int_0^\infty x^\beta P_L(x) dx = (e^{\sigma^2})^{\frac{\beta^2 - \beta}{2}} = \left(1 + \frac{1}{v}\right)^{\frac{\beta^2 - \beta}{2}}. \quad (21)$$

262 Figure 1b shows the rain rate based on the KK2000 parameterization scheme for the
 263 Gamma and Lognormal LWC PDF in Figure 1a. Interestingly, although the cumulative rain rates
 264 based on the two types of PDFs are almost identical, the contribution to the total rain rate from
 265 the different LWC bins are quite different. As show in Figure 1a, the $P_L(q_c)$ has a longer tail than
 266 the $P_G(q_c)$, i.e., the occurrence probability of large LWC (e.g., $q_c > 2.0 \text{ g/kg}$) is much higher in
 267 the Lognormal than in Gamma PDF. This difference is further amplified in the rain rate
 268 computation in Figure 1b because the rain rate is proportional to $q_c^{2.47}$.

269 The enhancement factors based on the Gamma (i.e., $E(P_G, \beta)$ in Eq. (20)) and Lognormal
 270 (i.e., $E(P_L, \beta)$ in Eq. (21)) PDF for $\beta_q = 2.47$ are plotted as a function of the inverse relative
 271 variance v in Figure 2. When subgrid clouds are more homogenous i.e., $v > 1$, the enhancement
 272 factor based on the two PDFs are similar. However, for more inhomogeneous grids with i.e., $v <$
 273 1, the $E(P_L, \beta)$ is significantly larger than that $E(P_G, \beta)$, which is probably because of the longer
 274 tail of $P_L(q_c)$ as shown in Figure 1 a and b.



275 It is important to note that not only the subgrid variation of q_c can lead to a nonlinear
276 effect on the simulation of autoconversion rate, the subgrid variation of N_c can have the same
277 effect. Physically, provided the same LWC, a cloud with smaller N_c would have larger droplet size
278 and therefore larger precipitation efficiency than the cloud with larger N_c . Because the
279 autoconversion rate depends nonlinearly on N_c , the grid-mean autoconversion rate computed
280 based on a skewed PDF of N_c (i.e., $\int_0^\infty (N_c)^{\beta_N} P(N_c) dN_c$) would be different from that computed
281 based on the mean of N_c (i.e., $(\langle N_c \rangle)^{\beta_N}$). The autoconversion enhancement factor based on the
282 Lognormal PDF $E(P_L, \beta)$ for $\beta_N = -1.79$ is given in Figure 2. Interestingly, at the same inverse
283 relative variance v , the enhancement factor based on the same Lognormal PDF $E(P_L, \beta)$ for $\beta_N =$
284 -1.79 is actually larger than that for $\beta_q = 2.47$ because of the formula of the exponent in Eq.
285 (21) (i.e., $\frac{\beta^2 - \beta}{2}$). This potentially important effect of the subgrid inhomogeneity of N_c on the
286 simulation of autoconversion rate has been overlooked or ignored in most previous studies. It is
287 perhaps partly because modeling N_c in GCM, especially its subgrid variation, is notoriously
288 difficult, and also partly because there is a lack of observation-based study of the subgrid
289 variation of N_c . One important objective of this study is to fill the second gap. We will use MODIS
290 observations to investigate the role of subgrid N_c variation on autoconversion simulation.

291 Finally, it has to be noted that when both q_c and N_c have significant subgrid variations,
292 their covariation also becomes important. As explained in Griffin and Larson (2013), if the q_c and
293 N_c are negatively correlated, clouds with larger q_c would tend to have smaller N_c . The
294 autoconversion rate in such a case would be larger than that in the case where q_c and N_c are
295 positively correlated (i.e., larger q_c would tend to have larger N_c). As explained in Eq. (17), only
296 when they are uncorrelated can the total enhancement factor be decomposed into the product
297 of two independent factors $E = E_q \cdot E_N$. Otherwise additional terms are necessary to take into
298 account the effect of q_c and N_c correlation. Although potentially important, the correlation of q_c
299 and N_c from satellite remote sensing data is difficult to derive from the satellite remote sensing
300 observations due to the retrieval uncertainties. We will return to this point later in Section 5.3.

301

302 3. Data and Methodology

303 Of particular interest to this study are the grid-mean value and subgrid variation of several



304 key properties of liquid-phase clouds, namely, COT, CER, LWP and CDNC, in the tropical regions.
305 For this purpose, we use the latest collection 6 (C6) *daily mean* level-3 cloud retrieval product
306 from the Aqua-MODIS instrument (product name “MYD08_D3”). The MODIS level-3 (i.e., grid-
307 level) product contains statistics computed from a set of level-2 (i.e., pixel-level) MODIS granules.
308 As summarized in (Platnick et al., 2003; 2017), the operational level-2 MODIS cloud product
309 provides cloud masking (Ackerman et al., 1998), cloud top height (Menzel et al., 1983), cloud top
310 thermodynamic phase determination (Menzel et al., 2006), and COT, CER and LWP retrievals
311 based on the bi-spectral solar reflectance method (Nakajima and King, 1990). All MODIS level-2
312 atmosphere products, including the cloud, aerosol and water vapor products, are aggregated to
313 $1^\circ \times 1^\circ$ spatial resolution on a daily, eight-day, and monthly basis. Aggregations include a variety
314 of scalar statistical information, including mean, standard deviation, max/min occurrences, as
315 well as histograms including both marginal and joint histograms. For COT, CER and LWP, the
316 MODIS level-3 product provides both their “in-cloud” grid-mean values ($\langle x \rangle$) and subgrid
317 standard deviations (σ_x). The inverse relative variance v can then be derived from Eq. (4), i.e.,
318 $v = \langle x \rangle^2 / \sigma_x^2$. Note that the operational MODIS product provides two CER retrievals, one based
319 on the observation from the band 7 centered around $2.1 \mu\text{m}$ and the other from band 20 at 3.7
320 μm . As discussed in several previous studies (Cho et al., 2015; Zhang and Platnick, 2011; Zhang
321 et al., 2012; 2016), the $3.7 \mu\text{m}$ band CER retrieval is more resilient to the 3-D effects and retrieval
322 failure than the $2.1 \mu\text{m}$ band retrievals. For these reasons, it is used as the observational
323 reference in this study.

324 Given the COT and CER retrieval, the operational MODIS product estimates the LWP of cloud
325 using

$$LWP = \frac{2}{3} \rho_w COT \cdot CER, \quad (22)$$

326 where ρ_w is the density of water. Several studies have argued that a smaller coefficient of $5/9$,
327 instead of $2/3$, should be used in estimation of LWP (Seethala and Horváth, 2010; Wood and
328 Hartmann, 2006). The choice of the coefficient has no impact on our study, because we are
329 interested in the relative inverse variance $v = \langle x \rangle^2 / \sigma_x^2$. We note here that it is the LWC, instead
330 of the LWP, that is used in the KK2000 scheme. So, the spatial variability of LWC is what is most



331 relevant. However, the remote sensing of cloud water vertical profile from satellite sensor for
332 liquid-phase clouds is extremely challenging even with active sensors. It is why most previous
333 studies using the satellite observations analyzed the spatial variation of LWP, rather than LWC.
334 In fact, even Lebsock et al. (2013), who used the level-2 CloudSat observations, had to use the
335 vertical averaged LWC in their analysis. Ground-based observations are much better than
336 satellite observation in this regard because they are closer to the target (i.e. clouds). Recently,
337 Xie and Zhang (2015) analyzed the cloud water profiles retrieved using ground-based radars from
338 the three ARM sites and found no obvious in-cloud vertical dependence of the spatial variability
339 of LWC. Following these previous studies, we assume that the horizontal subgrid variation of LWC
340 is *not* strongly dependent on height and its value can be inferred from the spatial variability of
341 the vertical integrated quantity LWP. The uncertainty caused by this assumption will be assessed
342 in future studies.

343 The current MODIS level-3 cloud product does *not* provide CDNC retrievals. Following
344 previous studies (Bennartz, 2007; Bennartz and Rausch, 2017; Grosvenor and Wood, 2014;
345 McCoy et al., 2017a), we estimate the CDNC (N_c) of liquid-phase clouds from the MODIS retrieved
346 COT (τ) and CER (r_e) based on the classic adiabatic cloud model

$$N_c(\tau, r_e) = \frac{\sqrt{5}}{2\pi k} \frac{\sqrt{f_{ad}\Gamma_w}}{\sqrt{\rho_w Q_e}} \tau^{\frac{1}{2}} r_e^{-\frac{5}{2}}, \quad (23)$$

347 where ρ_w is the density of water; $Q_e \approx 2$ is the extinction efficiency of cloud droplets; k is the
348 ratio of r_e to mean volume-equivalent radius; f_{ad} is the adiabaticity of the cloud; Γ_w is the LWC
349 lapse rate. Following previous studies, we assume $k = 0.8$ and $f_{ad} = 1.0$ to be constant and
350 compute Γ_w from the grid mean liquid cloud top temperature and pressure. The theoretical
351 basis and main uncertainty sources of the CDNC estimation based on the adiabatic cloud model
352 from MODIS-like passive cloud retrievals are nicely reviewed by Grosvenor et al. (2018).

353 Ideally, the values of *LWP* and CDNC should be estimated on pixel-by-pixel basis from the
354 level-2 MODIS product. However, pixel-by-pixel estimation is highly time consuming, which
355 makes it difficult to achieve a global perspective. Using an alternative method, many previous
356 studies estimate the grid-level CDNC statistics from the joint histogram of COT vs. CER provided



357 in the level-3 MODIS cloud products (Bennartz, 2007; McCoy et al., 2017a; 2017b). For a given
358 $1^\circ \times 1^\circ$ grid-box, the liquid-phase COT-CER joint histogram provides the counts of successful cloud
359 property retrievals with respect to 108 joint COT-CER bins that are bounded by 13 COT bin
360 boundaries, ranging from 0 to 150, and 10 CER bin boundaries, ranging from $4 \mu\text{m}$ to $30 \mu\text{m}$. With
361 the joint histogram, which is essentially the joint PDF of COT and CER $P(\tau, r_e)$, we can estimate
362 the grid mean and variance of CDNC from the following equations

$$\langle x \rangle = \int \int x(\tau, r_e) P(\tau, r_e) d\tau dr_e, \quad (24)$$

$$\text{Var}(x) = \int \int (x(\tau, r_e) - \langle N_c \rangle)^2 P(\tau, r_e) d\tau dr_e, \quad (25)$$

363 where x can be either LWP or CDNC. Figure 3a shows the LWP in Eq. (22) as a function of the 13
364 COT bins and 10 CER bins from the MODIS level-3 product. As expected, the largest LWP values
365 are found when both COT and CER are large. Figure 3b shows the CDNC in Eq. (23) as a function
366 of the COT and CER bins. As expected, the largest CDNC values are found when both COT is large
367 and CER is small. Figure 3c shows an example of the COT-CER joint histogram from the Aqua-
368 MODIS daily level-3 product “MYD08_D3” on January 09th, 2007 at the grid box 1°S and 1°W . In
369 this particular grid box, a combination of $2 \sim 4$ COT and $10 \mu\text{m} \sim 12 \mu\text{m}$ CER is the most frequently
370 observed cloud value. Using the joint histogram in Figure 3c, we can derive the mean and variance
371 of both LWP and COT using the Eqs. (24) and (25).

372 The efficiency of using the level-3 product is accompanied by two important limitations.
373 First, the current level-3 MODIS cloud product has a fixed $1^\circ \times 1^\circ$ spatial resolution. Although this
374 resolution is highly relevant to the current generation of GCMs, i.e., CMIP5 (Taylor et al., 2012),
375 future GCMs may have significantly finer resolution. Second, it is difficult to sub-sample the pixels
376 with the best retrieval quality. As reviewed in Grosvenor et al. (2018), the main source of
377 uncertainty in the CDNC retrieval is the MODIS retrieval uncertainties, particularly in CER because
378 of $N_c \sim r_e^{-\frac{5}{2}}$ dependence. In the pixel-by-pixel method, the pixel-level retrieval uncertainties, as
379 well as some other metrics such as the sub-pixel inhomogeneity index, provided in the level-2
380 product can be used to select the pixels with the best retrieval quality. Here, because we use the
381 static COT-CER joint histogram provided in the operational level-3 product, we do not have the



382 flexibility to sub-sample the data using retrieval quality. Alternatively, we can sub-sample the
383 data using the COT. It is well known that the bi-spectral retrieval method has a large uncertainty
384 for thin clouds. Indeed, the clouds with COT thinner than about 4 have often been screened out
385 in previous studies (Quaas et al., 2008). Such screening can be easily done with the joint PDF of
386 COT and CER, but it would obviously lead to sampling bias in LWP. The impact on CDNC is
387 dependent on whether the CDNC is correlated with the COT, i.e., whether thin clouds have the
388 similar CDNC as the thick clouds. We will revisit this point later. It should be noted that because
389 thin clouds in MODIS retrieval tend to have large uncertainty, any type of data quality-based data
390 screening would inevitably lead to the sampling bias.

391 4. Grid-mean and subgrid variations of liquid-phase cloud properties

392 The annual mean total cloud fraction (f_{tot}), liquid-phase cloud fraction (f_{liq}), in-cloud COT,
393 CER from the 3.7 μm band, LWP and estimated CDNC over the tropical oceans based on 10 years
394 Aqua-MODIS retrievals are shown in Figure 4. The highest f_{liq} in the tropics is usually found in the
395 stratocumulus (Sc) decks over the Eastern boundary of the ocean, e.g., SE Pacific off coast of Peru,
396 NE Pacific off the coast of California and SE Atlantic off the coast of Namibia. These regions are
397 associated with relatively low sea surface temperature (SST) due to cold upwelling ocean surface
398 current and mid-tropospheric subsidence of warm air from large-scale circulations, which
399 together lead to a strong low-tropospheric stability and high liquid-cloud fraction. With an annual
400 mean TOA cloud radiative effect usually around $-40 \sim -60 \text{ W/m}^2$, the Sc decks are important
401 modulators of the local and global radiative energy budget. The liquid-cloud fraction reduces
402 significantly toward the open ocean trade wind regions, where the dominate cloud types are
403 broken cumulus (Cu). Close to the continents, the Sc decks are susceptible to the influence of
404 continental air mass with higher loading of aerosols in comparison with pristine ocean
405 environment, which is probably the reason the SC decks have smaller CER and higher CDNC than
406 the open-ocean trade cumulus (Figure 4 d and f). The in-cloud COT (Figure 4 c) and LWP (Figure
407 4 e) generally increase from the Sc decks to the open-ocean Cu regime, although less dramatically
408 than the transition of cloud fraction. The Sc decks and the Sc-to-Cu transition are the most
409 prominent features of liquid-phase clouds in the tropics. However, as mentioned in the
410 introduction, simulating these features in the GCMs proves to be an extremely challenging task,



411 and most GCMs suffer from some common problems, such as the “too few too bright” problem
412 and the abrupt Sc-to-Cu transition problem (Kubar et al., 2014; Nam et al., 2012; Song et al.,
413 2018).

414 Switching the focus now from grid-mean values to subgrid variability, we show the grid-
415 level inverse relative variances $v = \langle x \rangle^2 / \text{Var}(x)$ for several key cloud properties. Recall that v
416 is defined such that the larger the v , the larger the mean value in comparison with the variance,
417 and the more homogeneous the cloud property within the grid. Because the value of v can be ill-
418 behaved when $\text{Var}(x)$ approaches zero, instead of the mean value, we plot the median value of
419 \tilde{v} based on 10 years of MODIS observations in Figure 5. There are several interesting and
420 important features in Figure 5. First of all, the \tilde{v} of all four sets of cloud properties (i.e., COT, CER,
421 LWP and CDNC) all exhibits a clear and similar Sc-to-Cu transition, with larger values in the Sc
422 region and smaller value in the broken Cu regions. This indicates that cloud properties, including
423 both optical and microphysical properties, are more homogenous, in terms of spatial distribution
424 within the grid, in the Sc region than in the Cu region. Secondly, the value of \tilde{v} of CER (i.e., 10~100
425 in Figure 5b) is larger than that of the other properties (i.e., 1~10) by almost an order of
426 magnitude, indicating that the subgrid variability of CER is very small. On the hand, however, it is
427 important to note that the \tilde{v} of CDNC (Figure 5d) is comparable with that of COT (Figure 5a) and
428 LWP (Figure 5c). The reason is probably in part because the highly nonlinear relationship between
429 CDNC and CER (i.e., $N_c \sim r_e^{-\frac{5}{2}}$) leads to a stronger variability of CDNC than CER, and also in part
430 because the variability of CDNC is also contributed by the subgrid variation of COT. In some
431 regions, the Gulf of Guinea, East and South China Sea, and Bay of Bengal for example, the \tilde{v} of
432 CDNC is close to unity, indicating the subgrid standard deviation of CDNC is comparable to the
433 grid-mean values in these regions. As discussed in the next section, the significant subgrid
434 variability of CDNC in these regions should be taken into account when modeling the nonlinear
435 processes, such as the auto-conversion, in GCM to avoid systematic biases due to the nonlinearity
436 effect.

437 The values of \tilde{v} in Figure 5 from this study are in reasonable agreement with previous
438 studies. Barker (1996) selected a few dozens of cloud scenes, each about 100 ~ 200 km in size,
439 from the Landsat observation and analyzed their spatial variability of COT. It is found that the



440 typical value of ν for “overcast stratocumulus”, “broken stratocumulus” and “scattered cumulus”
441 is 7.9, 1.2, and 0.7, respectively (see their Table 3), which is consistent with the Sc-to-Cu transition
442 pattern seen in Figure 5. Oreopoulos and Cahalan (2005) derived the subgrid inhomogeneity of
443 COT on a global scale from the level-3 Terra-MODIS retrievals. Although using a different metric
444 (i.e., their inhomogeneity parameter is defined as $\chi = \exp(\ln\langle\tau\rangle) / \langle\tau\rangle$), they also found
445 systematic increase of inhomogeneity (decreasing value of χ) from the Sc region to cu region.
446 Also using the MODIS cloud property retrievals, Wood and Hartmann(2006) investigated the
447 meso-scale spatial variability of LWP in the NE Pacific and SE Pacific region. The ν of LWP is found
448 to increase systematically with meso-scale cloud fraction and the relationship between the two
449 can be reasonably explained by a simple PDF cloud thickness model in Considine et al. (1997).
450 See also Kawai and Teixeira (2010).

451 5. Implications for warm-rain simulations in GCM

452 5.1. Influence of subgrid variation of LWP

453 As explained in the Theoretical Background, in GCMs the influences of subgrid cloud water
454 variability on the simulation of highly nonlinear autoconversion process are accounted for using
455 the enhancement factors defined in Eq. (15). For example, in CAM5.3, the MG cloud microphysics
456 parameterization scheme assumes that the subgrid cloud water follows the Gamma distribution
457 with the value of $\nu = 1$, which leads to a constant enhancement factor of 3.2 for the KK2000
458 autoconversion scheme (Morrison and Gettelman, 2008). Because its direct connection with the
459 precipitation rate, the enhancement factor can have significant impacts on precipitation, cloud,
460 and radiation fields of the host model. For the same reason, it is also often used as a “tuning”
461 parameter to optimize the model and reduce the differences between model simulations and
462 observations (Guo et al., 2014). Thus, an observational constraint on the enhancement factor is
463 of great interest to the modeling community and has been the target of several recent studies.
464 In the part 1 of a two-part study, Larson and Griffin (2013) present a theoretical framework based
465 on the joint PDF of cloud and meteorological properties for diagnosing the enhancement factors
466 for various nonlinear processes in warm clouds, e.g., autoconversion, accretion, and evaporation.
467 In part 2, Griffin and Larson (2013) analyzed the in situ measurements from the research flight
468 two (RF02) of the second Dynamics and Chemistry of Marine Stratocumulus (DYCOMS-II) field



469 experiment. It is found that taking into account the nonlinear effect caused by subgrid cloud
470 variability increases the autoconversion and accretion rates, leading to significantly more surface
471 precipitation and better agreement to the observations.

472 As discussed in Section 2.2, given the subgrid cloud property variations, we can derive the
473 enhancement factor using two approaches. In the first, we can derive the enhancement factor
474 based on its definition in Eq. (18) and (19) directly from the observed PDF of LWP or CDNC,
475 respectively. The advantage of this approach is that we do not have to make any assumption
476 about the shape of the subgrid cloud property variation (i.e., Gamma or Lognormal), although
477 this approach is more time consuming because it has to solve the integration. In the second
478 approach, we first derive the relative inverse relative variance v and then derive the
479 enhancement factor by assuming the subgrid PDF to be either Gamma (i.e., Eq. (20)) or
480 Lognormal (i.e., using Eq. (21)). This approach is more although it may be subject to significant
481 error if the true PDF deviates from the assumed PDF shape.

482 Figure 6a shows the median enhancement factor E_q in the tropical region derived based
483 on Eq. (18) (i.e., the first approach) from 10 years of MODIS observation. Figure 6 b and c show
484 the median enhancement factor E_q derived by assuming the subgrid cloud water follows the
485 Lognormal and Gamma distribution, respectively. There are a couple of interesting and important
486 points to note. First of all, similar to the grid-mean quantities in Figure 4, the enhancement factor
487 E_q also shows a clear Sc-to-Cu transition. Over the Sc decks, because clouds are more
488 homogeneous ($\tilde{v} > 5$), the enhancement factor E_q is only around $1 \sim 2.5$, while over the Cu
489 regions, the more inhomogeneous clouds with $\tilde{v} < 1$ leads to a larger enhancement factor E_q
490 around $3 \sim 5$. As aforementioned, in the current CAM5.3, E_q is assumed to be a constant of 3.2.
491 While this value is within the observational range, it obviously cannot capture the Sc-to-Cu
492 transition. In fact, the constant value 3.2 overestimates the E_q over the Sc region and
493 underestimates the E_q over the Cu region, which could lead to unrealistic drizzle product in both
494 regions and to consequential impacts on cloud water budget, radiation and even aerosol indirect
495 effects on the model. The second point to note is that the E_q based on the Lognormal PDF
496 assumption in Figure 6 b agrees well with the results in Figure 6 b derived directly from the
497 observation. In contrast, the E_q based on the Gamma PDF assumption in Figure 6 c tend to be



498 smaller, especially in the Cu regions. This result seems to suggest that the Lognormal distribution
499 provides a better fit to the observed subgrid cloud water variation than the Gamma distribution,
500 which has rarely been noted and reported in the previous studies.

501 A flexible, cloud-regime dependent E_q could help improve the simulation of Sc-to-Cu
502 transition in the GCM. If a GCM employs an advanced cloud parameterization scheme, such as
503 CLUBB, that is able to provide regime-dependent information on subgrid cloud variation, i.e., v ,
504 then the enhancement factor E_q could be diagnosed from v . However, most traditional cloud
505 parameterization schemes do not provide information on subgrid cloud variation. In such case, if
506 one does not wish to use a constant E_q , but a varying regime-dependent scheme, then either v
507 or E_q need to be parameterized as a function of some grid-mean cloud properties resolved by
508 the GCM. In facts, several attempts have been made along this line. Based on the combination
509 air-borne in situ measurement and satellite remote sensing product, Boutle et al. (2014)
510 parameterized the “fractional standard deviation” (which is equivalent to $1/\sqrt{v}$ in our definition)
511 of liquid-phase cloud as a function of grid-mean cloud fraction. This scheme was later updated
512 and tested in a host GCM in Hill et al. (2015), and was found to reduce the shortwave cloud
513 radiative forcing biases in the model. In a recent study, Xie and Zhang (2015) derived the subgrid
514 cloud variations from the ground-based observations from three Department of Energy (DOE)
515 Atmospheric Radiation Measurement (ARM) sites, and then parameterize the inverse relative
516 variance v as a function of the atmospheric stability.

517 Figure 7a shows the variation of inverse relative variance v as a function of the grid-mean
518 liquid-phase cloud fraction f_{liq} . In general, the value of v increases with the increasing f_{liq} , which
519 is expected from the Sc-to-Cu increase of f_{liq} in Figure 4b and the Sc-to-Cu decrease of v in Figure
520 5c. The $v(f_{liq})$ pattern in Figure 7a is also consistent with the results reported in Wood and
521 Hartmann (2006) and Lebsock et al. (2013). In the hope of obtaining a simple parameterization
522 scheme for $v(f_{liq})$ that can be used in GCMs, we fit the median value of v as a simple 3rd order
523 polynomial of f_{liq} as follows:

$$v(f_{liq}) = 2.38 - 4.95f_{liq} + 8.74f_{liq}^2 - 0.49f_{liq}^3, \quad f_{liq} \in (0,1]. \quad (26)$$



524 To test the performance of this simple parameterization, we first substitute the f_{liq} from MODIS
525 daily mean level-3 product into the above equation and then use the resultant v to compute the
526 enhancement factor E_q . Unfortunately, the median value of the enhancement factor E_q
527 computed based on the parameterized $v(f_{liq})$ as shown in Figure 8a substantially underestimate
528 the observation-based results in Figure 6, especially over the Cu regions. The deviation is
529 probably because the relationship between E_q and v is highly nonlinear (e.g., Eq. (20) and (21))
530 and therefore the above parameterization scheme that only fits the median value of v is not able
531 to capture the variability of E_q . Based on this consideration, we tried an alternative approach.
532 Instead of parameterization of v , we directly parameterize the enhancement factor E_q as a
533 function of f_{liq} . Figure 7b shows the variation of E_q as a function of f_{liq} . As expected, E_q generally
534 decreases with increasing f_{liq} . The median value of E_q is fitted with the following 3rd order
535 polynomial of f_{liq}

$$E_q(f_{liq}) = 2.72 + 7.33f_{liq} - 19.17f_{liq}^2 + 10.69f_{liq}^3, f_{liq} \in (0,1]. \quad (27)$$

536 As shown in Figure 8b, the median value of E_q based on the above equation clearly agrees with
537 the observation-based values in Figure 6 better than that based on the parameterization of
538 $v(f_{liq})$. The elimination of the middle step indeed improves the parameterization results. While
539 this is encouraging, it should be kept in mind that the Eq. (27) has very limited application, i.e., it
540 is only useful for the autoconversion rate computation for a particular value of the
541 autoconversion exponent beta, i.e., $\beta_q = 2.47$. A good parameterization of v could be useful for
542 not only autoconversion, but also for accretion and radiation computations. Another caution is
543 that, if applied to a GCM, the performance of the $E_q(f_{liq})$ parameterization in Eq. (27) will be
544 dependent on the simulated accuracy of f_{liq} in the model. In future study, we will implement this
545 parameterization scheme in a couple of GCMs and study the impacts on the cloud, precipitation
546 and radiation simulations. We will also explore better ways to parameterize the inverse relative
547 variance v .
548



549 5.2. Influence of subgrid variance of CDNC

550 In the previous section, we have mainly focused on the enhancement factor E_q on
551 autoconversion simulation due to the subgrid variation of cloud water. In this section we switch
552 the focus on the enhancement factor E_N due to the subgrid variation of CDNC.

553 The median value of E_N derived based on Eq. (19) from 10 years of MODIS observation is
554 shown in Figure 9a. There are several intriguing points to note. First of all, the value of E_N is
555 actually larger than E_q in Figure 9 such that we even have to use a different color scale for this
556 plot. Secondly, E_N the regions with escalated E_N seem to coincide with the downwind regions of
557 biomass burning aerosols (e.g., Gulf of Guinea, East Coast of South Africa), air pollution (i.e.,
558 Eastern China Sea), and, most interestingly, active volcanos (e.g., Kilauea Hawaii and Ambae
559 Vanuatu). We have also checked the seasonal variation of the E_N (shown in supplementary
560 materials) and the results also support this observation. Another interesting feature to note is
561 that, although the dust outflow regions such as Tropical East Atlantic and Arabian Sea, have heavy
562 aerosol loading, the value of E_N there is only moderate. Figure 9b shows the value of E_N
563 computed based on Eq. (21) from the inverse relative variance of v , assuming that the subgrid
564 CDNC follows a Lognormal PDF. Although the overall pattern is consistent with Figure 9a, the
565 assumption of Lognormal PDF seems to underestimate E_N . A closer examination indicates that
566 the Lognormal PDF tend to underestimate the population of clouds with small CDNC, and
567 therefore underestimate the variance of CDNC as well as E_N . We did not compute the E_N based
568 on the Gamma distribution because of the singular value problem aforementioned in Section 2.1.

569 We could not find any previous observation-based study on the global pattern of the
570 subgrid variation of CDNC and the corresponding E_N . So, it is difficult for us to corroborate our
571 results. On one hand, the pattern of E_N in Figure 9a seems to suggest that there are some
572 underlying physical mechanisms controlling the subgrid variation of CDNC, in which aerosols
573 seem to play an important role. On the other hand, the magnitude of E_N is surprisingly large. As
574 explained in section 3, the CDNC is estimated based on Eq. (23) from the MODIS retrieval of COT
575 and CER. Could retrieval uncertainty contribute to the large subgrid variation of CDNC and
576 therefore E_N ? In order to better understand the large value of E_N , we selected a case during the
577 biomass burning season in the Gulf of Guinea, which is shown in Figure 10. During the boreal



578 winter, the grassland and savanna fires in the southern West Africa generate a thick layer of
579 smoke aerosols that are clearly visible in the satellite image (Andreae and Merlet, 2001). On this
580 day, the Gulf of Guinea is quite cloudy, filled with broken cumulus clouds in the northern coastal
581 region and stratiform clouds in the south. We arbitrarily selected a smaller region, marked with
582 the red box, for detailed analysis. Although the cloud fraction in this region is about 60%, the
583 clouds are broken and optically thin with COT mostly smaller than 10. Interestingly, the CER varies
584 substantially from as low as $4 \mu\text{m}$ up to $30 \mu\text{m}$ in this relatively small region. Because of the highly
585 nonlinear dependence of CDNC on CER (i.e., $N_c \sim r_e^{-5/2}$), the large variance of CER leads to an
586 even larger variance of CDNC. The E_N derived based on Eq. (19) is 9.9. In contrast, the E_q is only
587 about 1.5.

588 The results from the above case study raises some concerns. It seems that the large
589 variations of CER and therefore CDNC are usually associated with thin clouds. While there could
590 be a physical explanation (e.g., CCN activation), it seems more likely to be caused, or at least
591 contributed, by retrieval uncertainty. It is well known that the bispectral method has large
592 uncertainties for thin clouds, especially when they are broken. Several previous studies have
593 shown that the sub-pixel level surface contamination, subpixel inhomogeneity, and three-
594 dimensional radiative transfer effects, tend to cause overestimated CER retrieval on top of large
595 uncertainties (Zhang and Platnick, 2011; Zhang et al., 2012; 2016). Therefore, for such a
596 challenging case in Figure 10, it is not surprising that the large CDNC variation and E_N are partly
597 caused by retrieval uncertainty. Based on this consideration, we did a sensitivity test, in which
598 we screen out the thin clouds with $\text{COT} < 4$ in the computation and analysis of CDNC and E_N . The
599 result from this test is shown in Figure 9c. Indeed, the removal of thin clouds substantially
600 reduces the value of E_N . For example, in the Gulf of Guinea, the median value of E_N reduces by
601 a factor of 4 from about 10 to only about 2.5. Nevertheless, the global pattern of E_N still remains,
602 i.e., nonnegligible values of E_N are found in the downwind regions of biomass burning, air
603 pollution and volcano emission.

604 As far as we know, the results in Figure 9 and Figure 10 mark the first attempt based on
605 satellite observations to unveil the global pattern of the subgrid variations of CDNC and
606 investigate the consequential impacts on warm rain simulations in GCMs. Although obscured by



607 satellite retrieval uncertainties, the results still provide several valuable insights. First of all, the
608 enhancement factor E_N due to the subgrid variations of CDNC is nonnegligible, even comparable
609 the effect of subgrid cloud water variation (i.e., E_q). Second, the global pattern of E_N in Figure 9
610 provides a valuable map for future studies, which in our opinion should focus on the regions with
611 large E_N , e.g., Gulf of Guinea, East Coast of South Africa and Eastern China Sea. Last, but not least,
612 the example in Figure 10 clearly exposes the limitation of the current satellite remote sensing
613 method. There are alternative methods for retrieving the CDNC from satellite observations (see
614 discussion in Grosvenor et al. (2018)). However, these methods more or less face the same
615 challenges as the MODIS retrieval (i.e., surface contamination, 3D effects). Future studies should
616 consider using the air-borne in situ measurements of cloud microphysics in the regions with
617 significant E_N , if available.

618 5.3. The combined effect of subgrid variations of cloud water and CDNC

619 As discussed in Section 2.2, the combined effect of the subgrid variations of cloud water
620 and CDNC can be derived from joint PDF $P(q, N_C)$ based on Eq. (15). Because both q and N_C are
621 a function of the retrieved COT and CER, we can easily derive the combined enhancement factor
622 E from the COT-CER joint histogram of MODIS product simply changing the integration domain
623 of Eq. (15) from q and N_C to COT and CER. The median value of the combined enhancement
624 factor E based on Eq. (15) is shown in Figure 11a. As one would expect, the combined
625 enhancement factor is generally larger than both E_q in Figure 6 and the E_N in Figure 9. It is easy
626 to see that the in some regions (e.g., Gulf of Guinea, East Coast of South Africa and Eastern China
627 Sea) the combined enhancement factor E resembles the E_N while in other regions (i.e., trade
628 wind cumulus regions over open ocean) it resembles more of E_q . Interestingly, because both E_q
629 and E_N are small over the Sc decks, those regions have the smallest combined enhancement
630 factor E .

631 As discussed in Section 2.2, only when the subgrid variation of cloud water is uncorrelated
632 with the subgrid variation of CDNC can the combined enhancement factor E be decomposed into
633 the simple product of E_q and E_N (i.e., Eq. (17)). Otherwise, additional terms that could be quite
634 complicated are needed to account for the effect of correlation (Lebsock et al., 2013). Here, we
635 performed a couple of simple tests to understand the potential correlation between E_q and E_N .



636 In the first test, we simply compare the product $E_q \cdot E_N$ with the observation-based E in Figure
637 11a and we found that the simple product $E_q \cdot E_N$ substantially overestimates E , especially over
638 the region with large E_N (not shown). In the light of the example in Figure 10, in the second test
639 we screened out the optical thin clouds and computed the $E_q \cdot E_N (COT > 4)$, which is shown in
640 Figure 11b. It should be clarified that optically thin clouds are kept in the computation of both E_q
641 and E , only left out in E_N . Apparently, the $E_q \cdot E_N (COT > 4)$ agrees reasonably well with the
642 combined enhancement factor in Figure 11a. This is encouraging on one hand, but on the other
643 not easy to explain. A possible explanation is that there is an apparent positive correlation
644 between cloud water and CDNC in the region with large E_N (i.e., optically thin clouds with less
645 cloud water tend to have larger CER and smaller CDNC). This correlation mainly exists among
646 optically thin clouds as a result of retrieval bias and uncertainty and it tends to counteract the
647 effect of E_q and E_N making the combined enhancement factor E substantially smaller than the
648 simple product of $E_q \cdot E_N$ (i.e., assuming no correlation).

649

650 6. Summary and Outlook

651 One of the difficulties in GCM simulation of the warm rain process is how to account for
652 the impact of subgrid variations of cloud properties, such as cloud water and CDNC, on nonlinear
653 precipitation processes such as autoconversion. In practice, this impact is often treated by adding
654 the enhancement factor term to the parameterization scheme. In this study, we derived the
655 subgrid variations of liquid-phase cloud properties over the tropical ocean using the satellite
656 remote sensing products from MODIS and investigated the corresponding enhancement factors
657 for parameterizations of autoconversion rate. In comparison with previous work, our study is
658 able to shed some new light on this problem in the following regards:

- 659 1. The wide spatial coverage of the Level-3 MODIS product enables us to depict a
660 detailed quantitative picture of the enhancement factor E_q due to the subgrid
661 variation of cloud water, which shows a clear cloud regime dependence, i.e., a Sc-
662 to-Cu increase. The constant $E_q = 3.2$ used in the current CAM5.3 model
663 overestimates and estimates the observed E_q in the Sc and Cu regions,
664 respectively.



- 665 2. The E_q based on the Lognormal PDF assumption performs slightly better than that
666 based on the Gamma PDF assumption.
- 667 3. A simple parameterization scheme is provided to relate E_q to the grid-mean liquid
668 cloud fraction, which can be readily used in GCMs.
- 669 4. For the first time, the enhancement factor E_N due to the subgrid variation of CDNC
670 is derived from satellite observation, and the results reveal several regions
671 downwind of biomass burning aerosols (e.g., Gulf of Guinea, East Coast of South
672 Africa), air pollution (i.e., Eastern China Sea), and active volcanos (e.g., Kilauea
673 Hawaii and Ambae Vanuatu), where the E_N is comparable, or even larger than
674 E_q , even after the optically thin clouds are screened out.

675 In future studies, we will further investigate the implications of these findings from
676 observations for warm rain simulations in GCMs. For example, the parameterization scheme of
677 $E_q(f_{liq})$ in Eq. (27) can be implemented in the GCMs and compared to the results based on the
678 constant E_q assumption to understand the potential influence of considering a cloud-regime-
679 dependent E_q on cloud simulations. Recently, a few novel methods have been developed to
680 provide certain information on the subgrid cloud property variations to the host GCM. Most
681 noticeable examples are the super-parameterization method (a.k.a. multi-scale modeling
682 framework) (Wang et al., 2015) and the higher-order turbulence closure methods (e.g., Cloud
683 Layer Unified By Binormals, CLUBB) (Golaz et al., 2002a; Guo et al., 2015; Larson et al., 2002).
684 Those GCMs coupled with these new schemes, theoretically, would no longer need the
685 enhancement factor. Nevertheless, the subgrid cloud property variations derived in this study
686 provide the observational basis for the evaluation and improvement of these schemes.

687 As noted in the previous sections, this study has several important limitations, most of
688 which are a result of using the level-3 MODIS observations. The fixed $1^\circ \times 1^\circ$ spatial resolution of
689 MODIS level-3 product makes it impossible for us to investigate the scale-dependence of subgrid
690 cloud variation. Similar to previous studies, we have to make several assumptions when
691 estimating the CDNC from level-3 MODIS product. Furthermore, the retrieval uncertainties
692 associated with the optically thin clouds in MODIS product pose a challenging obstacle for the
693 quantification of subgrid cloud property variations and the corresponding enhancement factors.



694 These limitations have to be addressed using additional independent observations from, for
695 example, ground based remote sensing product and/or in situ measurement from air-borne field
696 campaigns. Nevertheless, the results from this study provide a valuable roadmap for future
697 studies.

698 **Acknowledgement:**

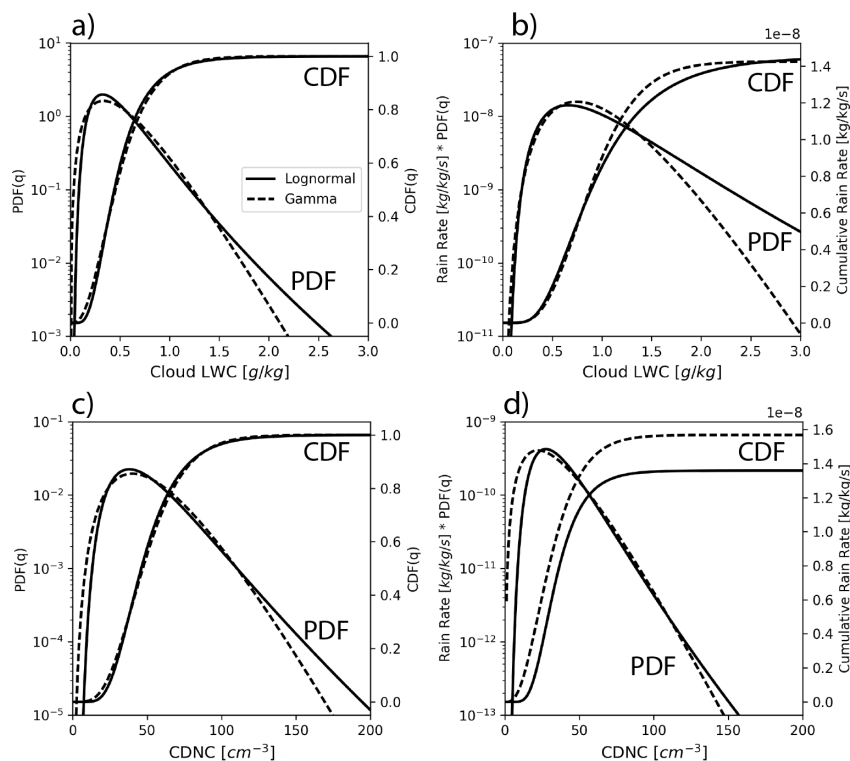
699 Z. Zhang acknowledges the financial support from the Regional and Global Climate Modeling
700 Program (Grant DE-SC0014641) funded by the Office of Biological and Environmental Research
701 in the US DOE Office of Science. V. Larson is grateful for financial support from Climate Model
702 Development and Validation grant DE-SC0016287, which is funded by the Office of Biological
703 and Environmental Research in the US DOE Office of Science. M. Wang was supported by the
704 Minister of Science and Technology of China (2017YFA0604001). The computations in this study
705 were performed at the UMBC High Performance Computing Facility (HPCF). The facility is
706 supported by the U.S. National Science Foundation through the MRI program (Grants CNS-
707 0821258 and CNS-1228778) and the SCREMS program (Grant DMS-0821311), with substantial
708 support from UMBC.

709



710

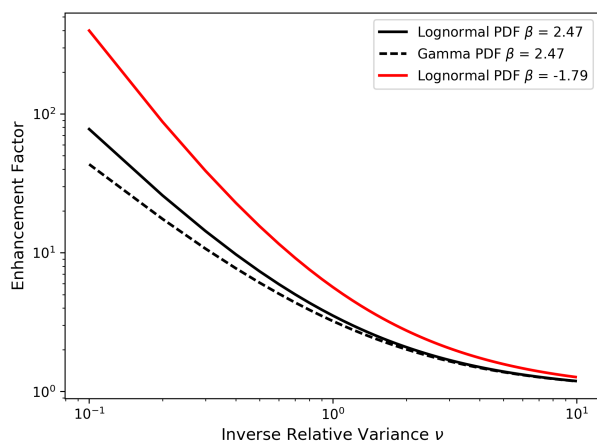
711 Figures:



712

713 *Figure 1* a) The PDF and cumulative distribution function (CDF) of cloud LWC that follow the
 714 Gamma (dashed) and Lognormal (solid) distribution. For the both distributions, $\langle LWC \rangle =$
 715 $0.5g/kg$ and $\nu = 3.0$. b) The PDF and CDF of rain rate computed based on the KK2000 scheme
 716 in Eq. (12) and the PDF of LWC. In the computation, the CDNC is kept at a constant of $50 cm^{-1}$.
 717 c) The PDF and CDF of CDNC that follow the Gamma (dashed) and Lognormal (solid)
 718 distribution. For the both distributions, $\langle N_c \rangle = 50 cm^{-3}$ and $\nu = 5.0$. d) the PDF and CDF of the
 719 rain rate computed based on the KK2000 scheme in Eq. (12) and the PDF of CDNC. The LWC is
 720 kept at $0.5g/kg$ in the computation.

721



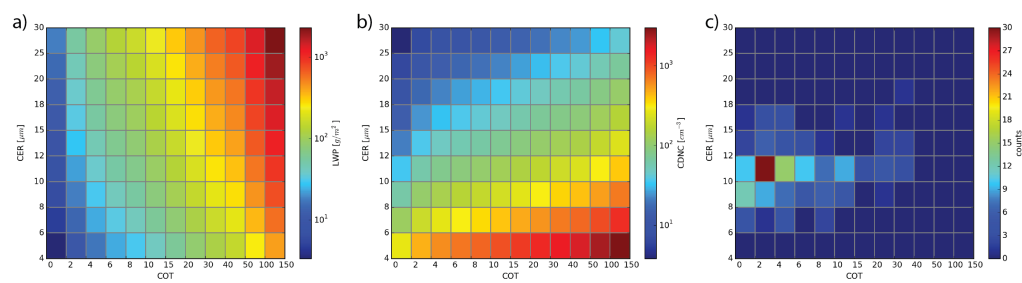
722

723 *Figure 2 Enhancement factors based on Lognormal $E(P_L, \beta)$ and Gamma $E(P_G, \beta)$ subgrid PDF*
724 *for different β as a function of the inverse relative variance v .*

725



726



727

728

729

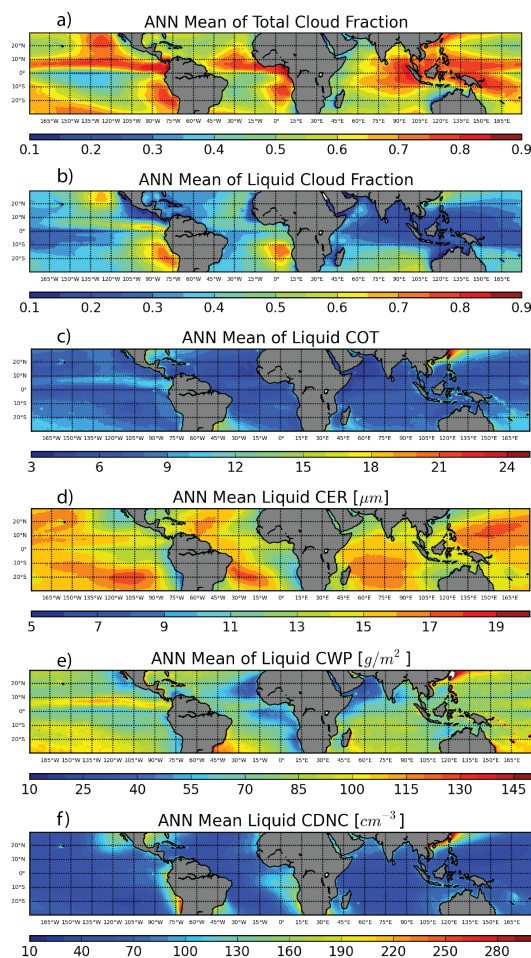
Figure 3 The (a) LWP and (b) CDNC as a function of COT and CER. (c) An example of the COT-CER joint histogram observed by Aqua-MODIS on Jan. 09th, 2007 at 1°S and 1°W.

730



731

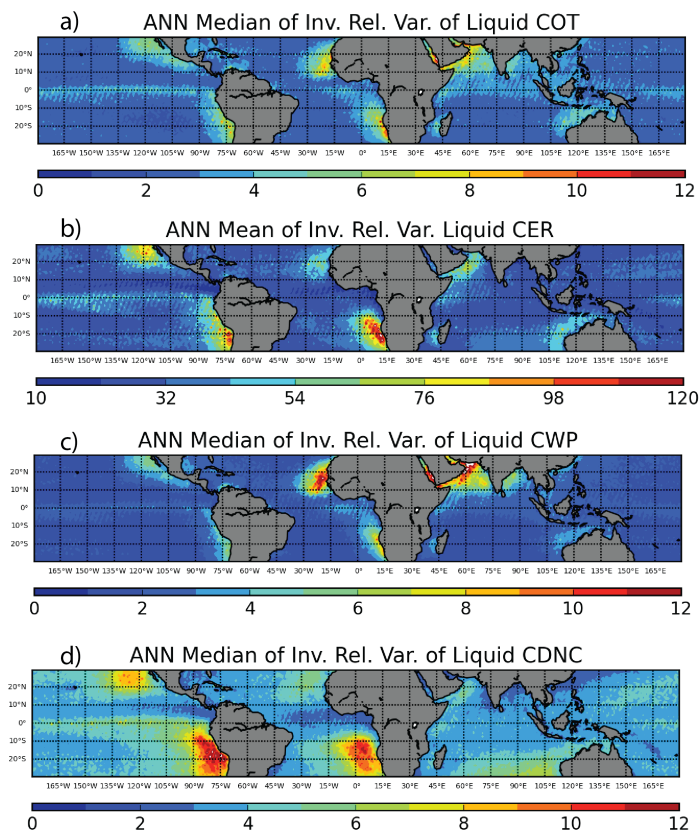
732



733

734 *Figure 4* 10-year (2007~2016) averaged annual mean a) total cloud fraction, b) liquid cloud
 735 fraction, c) cloud optical thickness, d) cloud effective radius retrieved from the 3.7 μm band, e)
 736 cloud water path and f) cloud droplet concentration retrievals from Aqua-MODIS over the
 737 tropical (30°S - 30°N) oceans. All quantities are “in-cloud” mean that are averaged over the
 738 cloudy-part of the grid only.

739



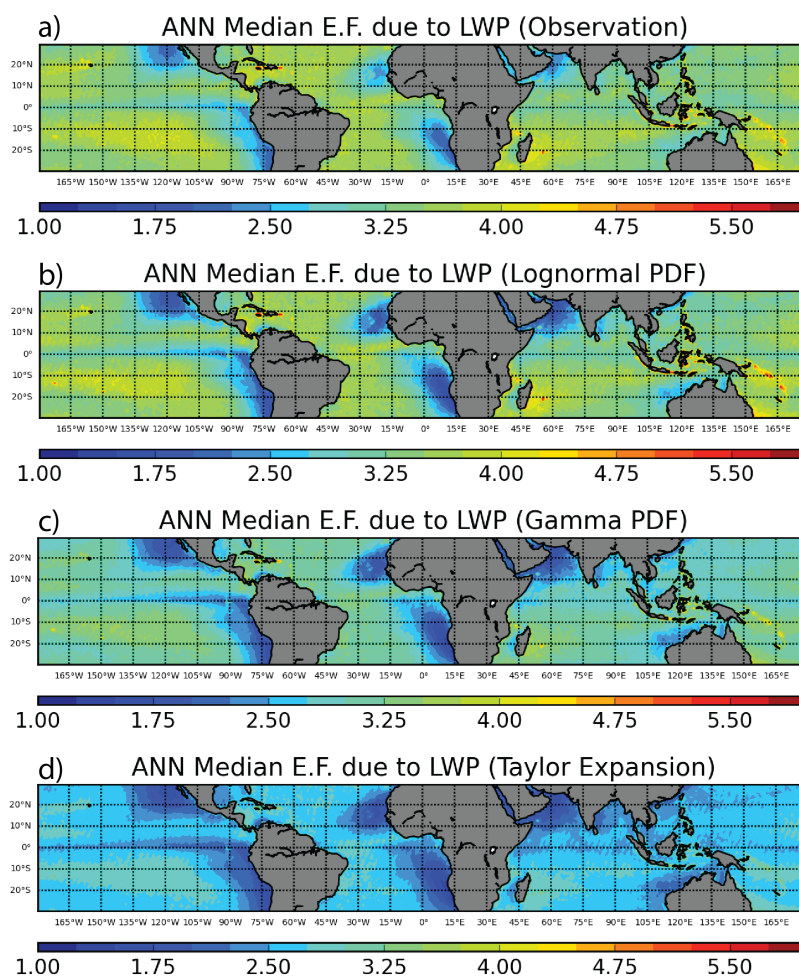
740

741 *Figure 5* 10-year (2007~2016) averaged annual mean inverse relative variance (i.e., $v =$
 742 $\langle x \rangle^2 / Var(x)$) of a) COT, b) CER, c) LWP and d) CDNC. Note that the color scale of CER is
 743 different from others'.

744



745



746

747

748 *Figure 6* The median enhancement factor for the KK2000 scheme due to subgrid variation of

749 LWP computed a) directly from observation, i.e., E_q in Eq. (17), b) from relative variance

750 assuming Lognormal PDF of LWP and c) from relative variance assuming the Gamma PDF of

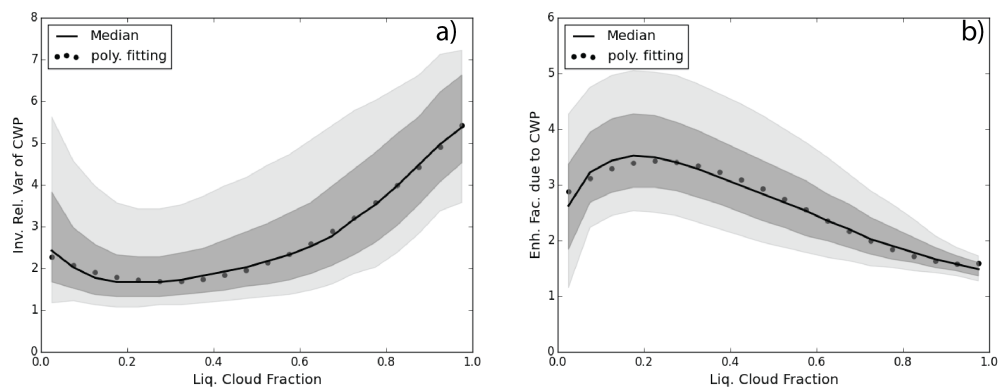
751 LWP.

752



752

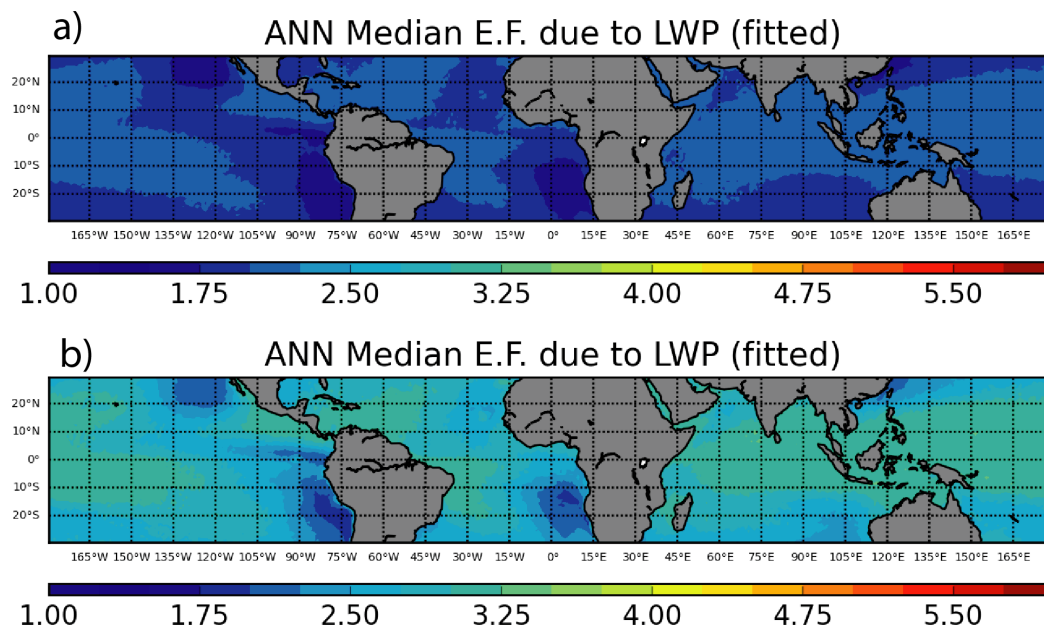
753



754

755 *Figure 7* a) The inverse relative variance v and b) autoconversion enhancement factor due to
756 LWP subgrid variability assuming Log-normal PDF as a function of grid-mean liquid cloud
757 fraction, where the solid line, dark shaded area, and light shaded area correspond to the
758 median value, 25%~75% percentiles, and 10~90% percentiles, respectively. The dotted lines
759 correspond to simple 3-rd order polynomial fitting.

760



761

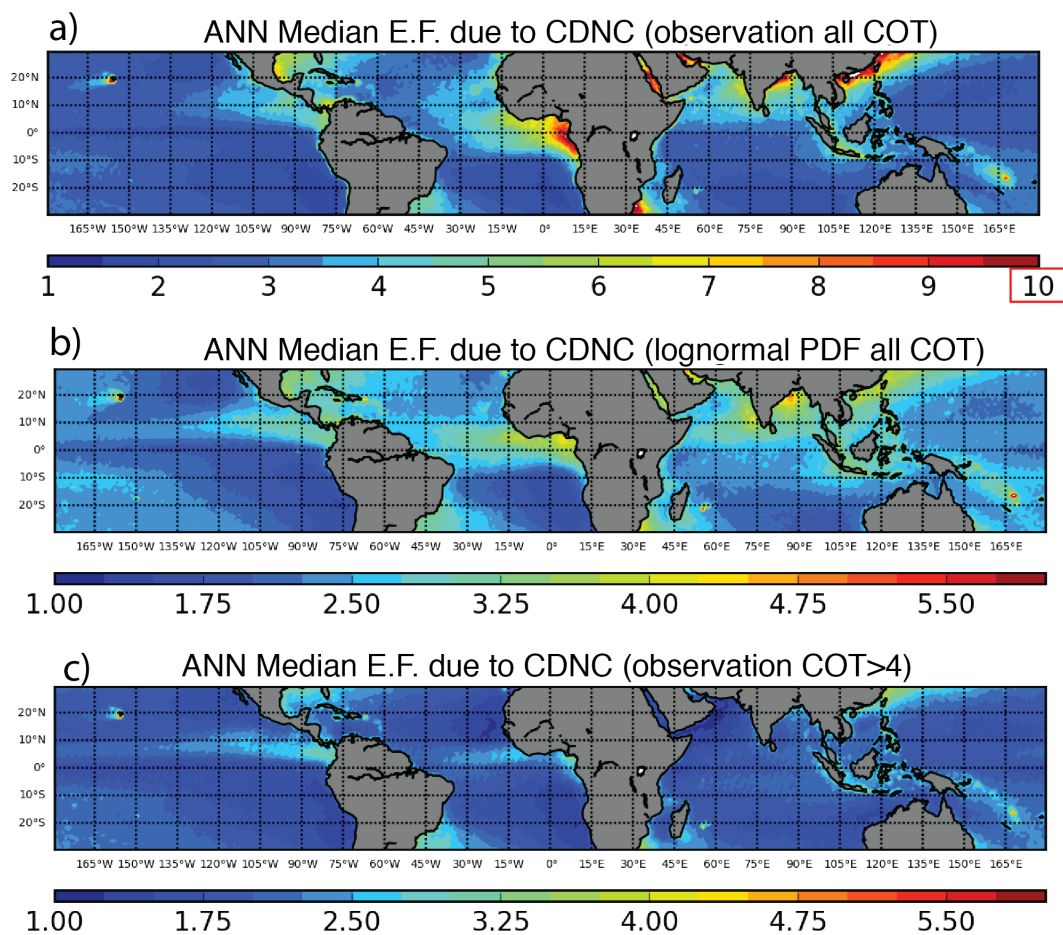
762 *Figure 8 Median value of the enhancement factor computed based on the a) $v(f_{liq})$*

763 *parameterization scheme in Eq. (26) and b) $E_q(f_{liq})$ parameterization scheme in Eq. (27).*

764

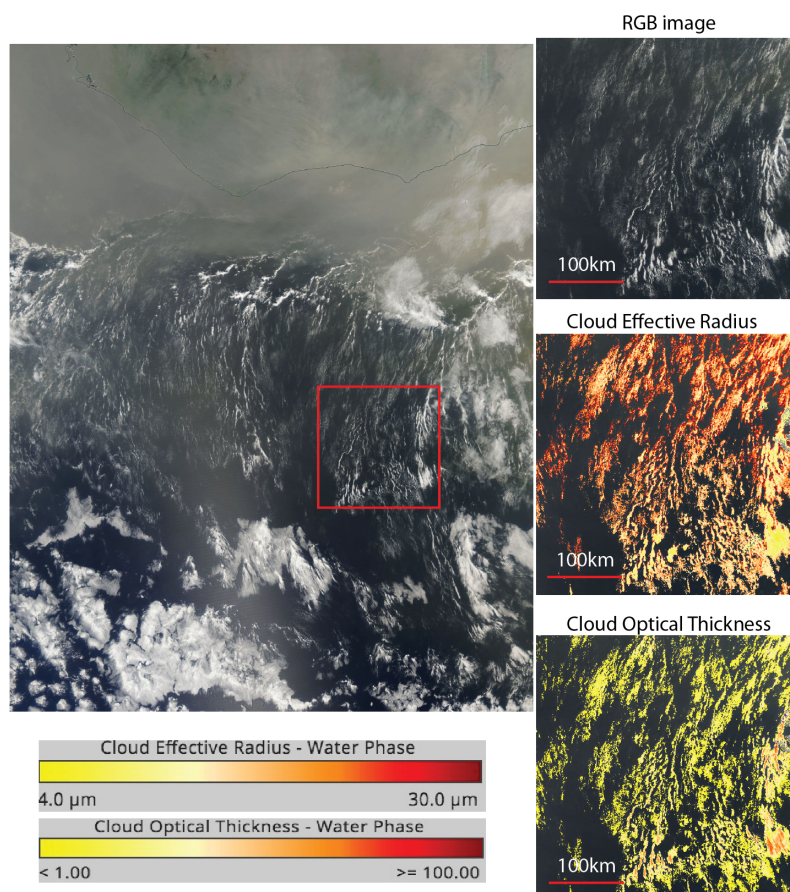


765
766
767



768
769
770
771
772

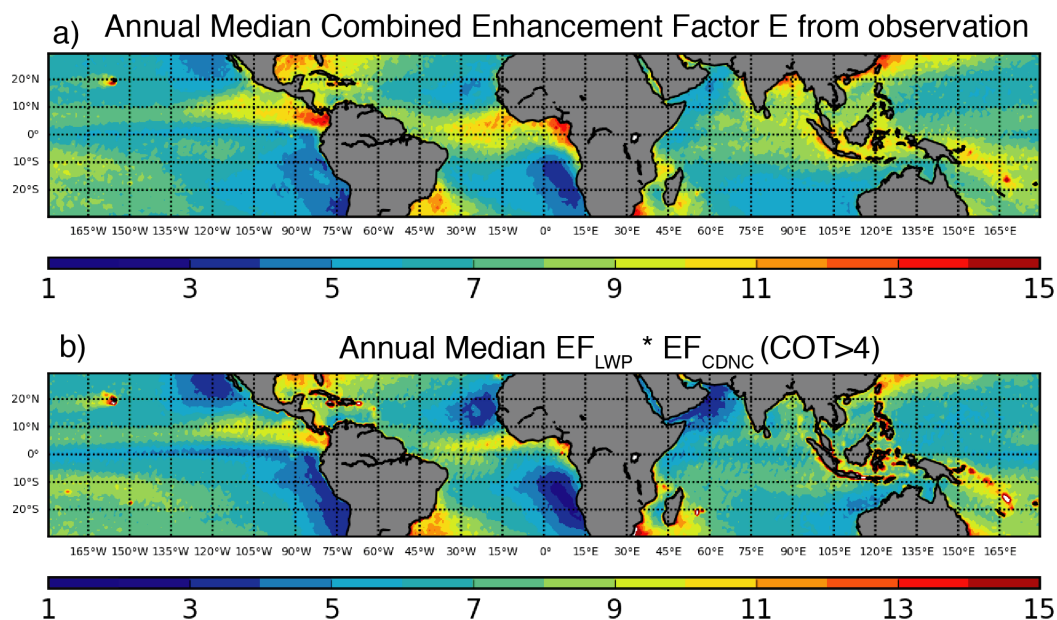
Figure 9 Median value of the enhancement factor E_N derived from a) observation based on Eq. (19) and b) from Eq. (21) assuming Lognormal subgrid CDNC distribution. c) same as a) except that thin clouds with $COT < 4$ have been screened out from the analysis.



773
774

775 *Figure 10 An example of the large E_N in the Gulf of Guinea observed by Aqua-MODIS on*
776 *Jan.09th, 2007. The large image on the left shows the true color image of the region. The three*
777 *smaller images on the right are, from top to bottom, the zoom-in RGB image, CER and COT*
778 *retrievals of the subregion in red box.*

779



780

781 *Figure 11 a) the combined enhancement factor based on Eq. (15), b) the combined*
 782 *enhancement factor based on the assumption that subgrid variations of LWP and CDNC are*
 783 *uncorrelated, i.e., $E_q \cdot E_N(COT > 4)$. Optical thin clouds ($COT < 4$) are screened out in the*
 784 *computation of E_N to reduce the impact of retrieval artifacts.*

785

786



787

788

789 **Reference:**

790 Ackerman, S., Strabala, K., Menzel, W., Frey, R., Moeller, C. and Gumley, L.: Discriminating clear
791 sky from clouds with MODIS, *Journal of Geophysical Research*, 103(D24), 32,141–32,157, 1998.

792 Andreae, M. O. and Merlet, P.: Emission of trace gases and aerosols from biomass burning,
793 *Global Biogeochemical Cycles*, 15(4), 955–966, doi:10.1029/2000GB001382, 2001.

794 Barker, H. W.: A Parameterization for Computing Grid-Averaged Solar Fluxes for
795 Inhomogeneous Marine Boundary Layer Clouds. Part I: Methodology and Homogeneous Biases,
796 *J. Atmos. Sci.*, 53(16), 2289–2303, doi:10.1175/1520-0469(1996)053<2289:APFCGA>2.0.CO;2,
797 1996.

798 Barker, H. W., Wiellicki, B. A. and Parker, L.: A Parameterization for Computing Grid-Averaged
799 Solar Fluxes for Inhomogeneous Marine Boundary Layer Clouds. Part II: Validation Using
800 Satellite Data, [http://dx.doi.org/10.1175/1520-0469\(1996\)053<2304:APFCGA>2.0.CO;2](http://dx.doi.org/10.1175/1520-0469(1996)053<2304:APFCGA>2.0.CO;2), 53(16),
801 2304–2316 [online] Available from: [http://journals.ametsoc.org/doi/pdf/10.1175/1520-](http://journals.ametsoc.org/doi/pdf/10.1175/1520-0469%281996%29053%3C2304%3AAPFCGA%3E2.0.CO%3B2)
802 [0469%281996%29053%3C2304%3AAPFCGA%3E2.0.CO%3B2](http://journals.ametsoc.org/doi/pdf/10.1175/1520-0469%281996%29053%3C2304%3AAPFCGA%3E2.0.CO%3B2), 1996.

803 Bennartz, R.: Global assessment of marine boundary layer cloud droplet number concentration
804 from satellite, *Journal of Geophysical Research-Atmospheres*, 2007.

805 Bennartz, R. and Rausch, J.: Global and regional estimates of warm cloud droplet number
806 concentration based on 13 years of AQUA-MODIS observations, *Atmospheric Chemistry and*
807 *Physics*, 1–32, doi:10.5194/acp-2016-1130, 2017.

808 Bogenschutz, P. A., Gettelman, A., MORRISON, H., Larson, V. E., Craig, C. and Schanen, D. P.:
809 Higher-Order Turbulence Closure and Its Impact on Climate Simulations in the Community
810 Atmosphere Model, *J. Climate*, 26(23), 9655–9676, doi:10.1175/JCLI-D-13-00075.1, 2013.

811 Bony, S. and Dufresne, J.-L.: Marine boundary layer clouds at the heart of tropical cloud
812 feedback uncertainties in climate models, *Geophysical Research Letters*, 32(20), L20806,
813 doi:10.1029/2005GL023851, 2005.

814 Boutle, I. A. and Abel, S. J.: Microphysical controls on the stratocumulus topped boundary-layer
815 structure during VOCALS-REX, *Atmospheric Chemistry and Physics*, 12(6), 2849–2863,
816 doi:10.5194/acp-12-2849-2012, 2012.

817 Boutle, I. A., Abel, S. J., Hill, P. G. and Morcrette, C. J.: Spatial variability of liquid cloud and rain:
818 observations and microphysical effects, *Quarterly Journal of the Royal Meteorological Society*,
819 140(679), 583–594, doi:10.1002/qj.2140, 2014.



- 820 Cahalan, R. F., Ridgway, W., Wiscombe, W. J., Bell, T. L. and Snider, J. B.: The Albedo of Fractal
821 Stratocumulus Clouds, *J. Atmos. Sci.*, 51(16), 2434–2455, doi:10.1175/1520-
822 0469(1994)051<2434:TAOFSC>2.0.CO;2, 1994.
- 823 Cho, H. M., Zhang, Z., Meyer, K., Lebsock, M., Platnick, S., Ackerman, A. S., Di Girolamo, L., C
824 Labonnote, L., Cornet, C., Riedi, J. and Holz, R. E.: Frequency and causes of failed MODIS cloud
825 property retrievals for liquid phase clouds over global oceans, *Journal of Geophysical Research-*
826 *Atmospheres*, 120(9), 2015JD023161–n/a, doi:10.1002/2015JD023161, 2015.
- 827 Considine, G., Curry, J. A. and Wielicki, B.: Modeling cloud fraction and horizontal variability in
828 marine boundary layer clouds, *J. Geophys. Res.*, 102(D12), 13517–13525, 1997.
- 829 Golaz, J.-C., Larson, V. E. and Cotton, W. R.: A PDF-Based Model for Boundary Layer Clouds. Part
830 I: Method and Model Description, *JAS*, 59(24), 3540–3551, doi:10.1175/1520-
831 0469(2002)059<3540:APBMFB>2.0.CO;2, 2002a.
- 832 Golaz, J.-C., Larson, V. E. and Cotton, W. R.: A PDF-Based Model for Boundary Layer Clouds. Part
833 II: Model Results, [http://dx.doi.org/10.1175/1520-0469\(2002\)059<3552:APBMFB>2.0.CO;2](http://dx.doi.org/10.1175/1520-0469(2002)059<3552:APBMFB>2.0.CO;2),
834 59(24), 3552–3571, doi:10.1175/1520-0469(2002)059<3552:APBMFB>2.0.CO;2, 2002b.
- 835 Griffin, B. M. and Larson, V. E.: Analytic upscaling of a local microphysics scheme. Part II:
836 Simulations, *Quarterly Journal of the Royal Meteorological Society*, 139(670), 58–69,
837 doi:10.1002/qj.1966, 2013.
- 838 Grosvenor, D. P. and Wood, R.: The effect of solar zenith angle on MODIS cloud optical and
839 microphysical retrievals within marine liquid water clouds, *Atmospheric Chemistry and Physics*,
840 14(14), 7291–7321, doi:10.5194/acpd-14-303-2014, 2014.
- 841 Grosvenor, D. P., Sourdeval, O., Zuidema, P., Ackerman, A., Alexandrov, M. D., Bennartz, R.,
842 Cairns, B., Chiu, C., Christensen, M., Diamond, M., Feingold, G., Fridlind, A., Hunerbein, A., Knist,
843 C., Kollias, P., Marshak, A., McCoy, D., Merk, D., Painemal, D., Rausch, J., Rosenfeld, D.,
844 Russchenberg, H., Seifert, P., Sinclair, K., Stier, P., vanDiedenhoven, B., Wendisch, M., Werner,
845 F., Wood, R., Zhang, Z. and Quaas, J.: **Remote sensing of droplet number concentration in
846 warm clouds: A review of the current state of knowledge and perspectives**, *Reviews of
847 Geophysics*, (in review), 2018.
- 848 Gultepe, I. and Isaac, G. A.: Aircraft observations of cloud droplet number concentration:
849 Implications for climate studies, *Quarterly Journal of the Royal Meteorological Society*,
850 130(602), 2377–2390, doi:10.1256/qj.03.120, 2004.
- 851 Guo, H., Golaz, J. C., Donner, L. J., Wyman, B., Zhao, M. and Ginoux, P.: CLUBB as a unified cloud
852 parameterization: Opportunities and challenges, *Geophysical Research Letters*, 42(11), 4540–
853 4547, doi:10.1002/2015GL063672, 2015.
- 854 Guo, Z., Wang, M., Qian, Y., Larson, V. E., Ghan, S., Ovchinnikov, M., Bogenschutz, P. A., Zhao,
855 C., Lin, G. and Zhou, T.: A sensitivity analysis of cloud properties to CLUBB parameters in the



- 856 single-column Community Atmosphere Model (SCAM5), *J. Adv. Model. Earth Syst.*, 6(3), 829–
857 858, doi:10.1002/2014MS000315, 2014.
- 858 Hill, P. G., Morcrette, C. J. and Boutle, I. A.: A regime-dependent parametrization of subgrid-
859 scale cloud water content variability, *Quarterly Journal of the Royal Meteorological Society*,
860 141(691), 1975–1986, doi:10.1002/qj.2506, 2015.
- 861 Kawai, H. and Teixeira, J.: Probability Density Functions of Liquid Water Path and Cloud Amount
862 of Marine Boundary Layer Clouds: Geographical and Seasonal Variations and Controlling
863 Meteorological Factors, <http://dx.doi.org/10.1175/2009JCLI3070.1>, 23(8), 2079–2092,
864 doi:10.1175/2009JCLI3070.1, 2010.
- 865 Khairoutdinov, M. and Kogan, Y.: A New Cloud Physics Parameterization in a Large-Eddy
866 Simulation Model of Marine Stratocumulus, *Mon. Wea. Rev.*, 128(1), 229–243 [online] Available
867 from: [http://journals.ametsoc.org/doi/abs/10.1175/1520-](http://journals.ametsoc.org/doi/abs/10.1175/1520-0493(2000)128%3C0229%3AANCPPI%3E2.0.CO%3B2)
868 [0493\(2000\)128%3C0229%3AANCPPI%3E2.0.CO%3B2](http://journals.ametsoc.org/doi/abs/10.1175/1520-0493(2000)128%3C0229%3AANCPPI%3E2.0.CO%3B2), 2000.
- 869 Klein, S. and Hartmann, D.: The seasonal cycle of low stratiform clouds, *Journal of Climate*, 6(8),
870 1587–1606, 1993.
- 871 Kubar, T. L., Stephens, G. L., Lebsock, M., Larson, V. E. and Bogenschutz, P. A.: Regional
872 Assessments of Low Clouds against Large-Scale Stability in CAM5 and CAM-CLUBB Using MODIS
873 and ERA-Interim Reanalysis Data, *J. Climate*, 28(4), 1685–1706, doi:10.1175/JCLI-D-14-00184.1,
874 2014.
- 875 Larson, V. E. and Griffin, B. M.: Analytic upscaling of a local microphysics scheme. Part I:
876 Derivation, *Quarterly Journal of the Royal Meteorological Society*, 139(670), 46–57,
877 doi:10.1002/qj.1967, 2013.
- 878 Larson, V. E., Golaz, J.-C. and Cotton, W. R.: Small-Scale and Mesoscale Variability in Cloudy
879 Boundary Layers: Joint Probability Density Functions, *J. Atmos. Sci.*, 59(24), 3519–3539,
880 doi:10.1175/1520-0469(2002)059<3519:SSAMVI>2.0.CO;2, 2002.
- 881 Larson, V. E., Wood, R., Field, P. R., Golaz, J.-C., Vonder Haar, T. H. and Cotton, W. R.: Systematic
882 Biases in the Microphysics and Thermodynamics of Numerical Models That Ignore Subgrid-Scale
883 Variability, *J. Atmos. Sci.*, 58(9), 1117–1128, doi:10.1175/1520-
884 [0469\(2001\)058<1117:SBITMA>2.0.CO;2](http://journals.ametsoc.org/doi/abs/10.1175/1520-0469(2001)058<1117:SBITMA>2.0.CO;2), 2001.
- 885 Lebsock, M., MORRISON, H. and Gettelman, A.: Microphysical implications of cloud-
886 precipitation covariance derived from satellite remote sensing, *Journal of Geophysical*
887 *Research-Atmospheres*, 118(12), 6521–6533, doi:10.1002/jgrd.50347, 2013.
- 888 Lee, S., Kahn, B. H. and Teixeira, J.: Characterization of cloud liquid water content distributions
889 from CloudSat, *J. Geophys. Res.*, 115(D20), D00A23, doi:10.1029/2009JD013272, 2010.



- 890 McCoy, D. T., Bender, F. A. M., Grosvenor, D. P., Mohrmann, J. K., Hartmann, D. L., Wood, R.
891 and Field, P. R.: Predicting decadal trends in cloud droplet number concentration using
892 reanalysis and satellite data, *Atmospheric Chemistry and Physics*, 1–21, 2017a.
- 893 McCoy, D. T., Bender, F. A. M., Mohrmann, J. K. C., Hartmann, D. L., Wood, R. and Grosvenor, D.
894 P.: The global aerosol-cloud first indirect effect estimated using MODIS, MERRA, and AeroCom,
895 *Journal of Geophysical Research-Atmospheres*, 122(3), 1779–1796, doi:10.1002/2016JD026141,
896 2017b.
- 897 Menzel, P., Frey, R., Baum, B. and Zhang, H.: Cloud Top Properties and Cloud Phase Algorithm
898 Theoretical Basis Document. 2006.
- 899 Menzel, W., Smith, W. and Stewart, T.: Improved Cloud Motion Wind Vector and Altitude
900 Assignment Using VAS, *Journal of Applied Meteorology*, 22(3), 377–384, 1983.
- 901 Morales, R. and Nenes, A.: Characteristic updrafts for computing distribution-averaged cloud
902 droplet number and stratocumulus cloud properties, *J. Geophys. Res.*, 115(D18), 1227, 2010.
- 903 Morrison, H. and Gettelman, A.: A new two-moment bulk stratiform cloud microphysics scheme
904 in the Community Atmosphere Model, version 3 (CAM3). Part I: Description and numerical
905 tests, *Journal of Climate*, 2008.
- 906 Nakajima, T. and King, M. D.: Determination of the Optical Thickness and Effective Particle
907 Radius of Clouds from Reflected Solar Radiation Measurements. Part I: Theory, *J. Atmos. Sci.*,
908 47(15), 1878–1893, doi:10.1175/1520-0469(1990)047<1878:DOTOTA>2.0.CO;2, 1990.
- 909 Nam, C., Bony, S., Dufresne, J. L. and Chepfer, H.: The “too few, too bright” tropical low-cloud
910 problem in CMIP5 models, *Geophysical Research ...*, doi:10.1029/2012GL053421, 2012.
- 911 Oreopoulos, L. and Barker, H. W.: Accounting for subgrid-scale cloud variability in a multi-layer
912 1d solar radiative transfer algorithm, *Quarterly Journal of the Royal Meteorological Society*,
913 125(553), 301–330, doi:10.1002/qj.49712555316, 1999.
- 914 Oreopoulos, L. and Cahalan, R. F.: Cloud Inhomogeneity from MODIS, *Journal of Climate*,
915 18(23), 5110–5124, doi:10.1175/JCLI3591.1, 2005.
- 916 Oreopoulos, L. and Davies, R.: Plane Parallel Albedo Biases from Satellite Observations. Part I:
917 Dependence on Resolution and Other Factors, *Journal of Climate*, 11(5), 919–932, 1998a.
- 918 Oreopoulos, L. and Davies, R.: Plane Parallel Albedo Biases from Satellite Observations. Part II:
919 Parameterizations for Bias Removal, *J. Climate*, 11(5), 933–944, 1998b.
- 920 Pincus, R. and Klein, S. A.: Unresolved spatial variability and microphysical process rates in
921 large-scale models, *J. Geophys. Res.*, 105(D22), 27059–27065, doi:10.1029/2000JD900504,
922 2000.



- 923 Platnick, S., King, M. D., Ackerman, S. A., Menzel, W. P., Baum, B. A., Riédi, J. C. and Frey, R. A.:
924 The MODIS cloud products: algorithms and examples from Terra, IEEE TRANSACTIONS ON
925 GEOSCIENCE AND REMOTE SENSING, 41(2), 459–473, doi:10.1109/TGRS.2002.808301, 2003.
- 926 Platnick, S., Meyer, K. G., King, M. D., Wind, G., Amarasinghe, N., Marchant, B., Arnold, G. T.,
927 Zhang, Z., Hubanks, P. A., Holz, R. E., Yang, P., Ridgway, W. L. and Riedi, J.: The MODIS Cloud
928 Optical and Microphysical Products: Collection 6 Updates and Examples From Terra and Aqua,
929 IEEE TRANSACTIONS ON GEOSCIENCE AND REMOTE SENSING, 55(1), 502–525,
930 doi:10.1109/TGRS.2016.2610522", "rightsLink": "http://s100.copyright.com/AppDispatchServlet
931 ?publisherName=ieee&publication=0196-
932 2892&title=The+MODIS+Cloud+Optical+and+Microphysical+Products%3A+Collection+6+Updat
933 es+and+Examples+From+Terra+and+Aqua&isbn=&publicationDate=Jan.+2017&author=Steven+
934 Platnick&ContentID=10.1109/TGRS.2016.2610522&orderBeanReset=true&startPage=502&end
935 Page=525&volumeNum=55&issueNum=1", "displayPublicationTitle": "IEEE, 2017.
- 936 Pruppacher, H. R. and Klett, J. D.: Microphysics of Clouds and Precipitation: With an
937 Introduction to Cloud Chemistry and Cloud Electricity, 954 pp. 1997.
- 938 Quaas, J., Boucher, O., Bellouin, N. and Kinne, S.: Satellite-based estimate of the direct and
939 indirect aerosol climate forcing, J. Geophys. Res., 113(D5), n/a–n/a,
940 doi:10.1029/2007JD008962, 2008.
- 941 Seethala, C. and Horváth, Á.: Global assessment of AMSR-E and MODIS cloud liquid water path
942 retrievals in warm oceanic clouds, J Geophys Res, 115(D13), D13202, 2010.
- 943 Soden, B. and Held, I.: An assessment of climate feedbacks in coupled ocean–atmosphere
944 models, Journal of Climate, 2006.
- 945 Song, H., Song, H., Zhang, Z., Ma, P.-L., Ghan, S. J. and Wang, M.: An Evaluation of Marine
946 Boundary Layer Cloud Property Simulations in the Community Atmosphere Model Using
947 Satellite Observations: Conventional Subgrid Parameterization versus CLUBB, Journal of
948 Climate, 31(6), 2299–2320, doi:10.1175/JCLI-D-17-0277.1, 2018.
- 949 Song, H., Zhang, Z., Ma, P. L., Ghan, S. and Wang, M.: An Evaluation of Marine Boundary Layer
950 Cloud Property Simulations in Community Atmosphere Model Using Satellite Observations:
951 Conventional Sub-grid Parameterization vs. CLUBB, J. Climate, JCLI–D–17–0277.1,
952 doi:10.1175/JCLI-D-17-0277.1, 2017.
- 953 Taylor, K. E., Stouffer, R. J. and Meehl, G. A.: An Overview of CMIP5 and the Experiment Design,
954 Bulletin of the American Meteorological Society, 93(4), 485–498, doi:10.1175/BAMS-D-11-
955 00094.1, 2012.
- 956 Thayer-Calder, K., Gettelman, A., Craig, C., Goldhaber, S., Bogenschütz, P. A., Chen, C. C.,
957 Morrison, H., Höft, J., Raut, E., Griffin, B. M., Weber, J. K., Larson, V. E., Wyant, M. C., Wang, M.,
958 Guo, Z. and Ghan, S. J.: A unified parameterization of clouds and turbulence using CLUBB and



- 959 subcolumns in the Community Atmosphere Model, *Geosci. Model Dev.*, 8(12), 3801–3821,
960 doi:10.5194/gmd-8-3801-2015, 2015.
- 961 Trenberth, K. E., Fasullo, J. T. and Kiehl, J.: Earth's Global Energy Budget, *Bull. Amer. Meteor.*
962 *Soc.*, 90(3), 311–323, doi:10.1175/2008BAMS2634.1, 2009.
- 963 Wang, M., Larson, V. E., Ghan, S., Ovchinnikov, M., Schanen, D. P., Xiao, H., Liu, X., Rasch, P. and
964 Guo, Z.: A multiscale modeling framework model (superparameterized CAM5) with a higher-
965 order turbulence closure: Model description and low-cloud simulations, *J. Adv. Model. Earth*
966 *Syst.*, n/a–n/a, doi:10.1002/2014MS000375, 2015.
- 967 Wood, R. and Hartmann, D.: Spatial variability of liquid water path in marine low cloud: The
968 importance of mesoscale cellular convection, *Journal of Climate*, 2006.
- 969 Xie, X. and Zhang, M.: Scale-aware parameterization of liquid cloud inhomogeneity and its
970 impact on simulated climate in CESM, *Journal of Geophysical Research-Atmospheres*, 120(16),
971 8359–8371, doi:10.1002/2015JD023565, 2015.
- 972 Zhang, Z. and Platnick, S.: An assessment of differences between cloud effective particle radius
973 retrievals for marine water clouds from three MODIS spectral bands, *J Geophys Res*, 116(D20),
974 D20215, doi:10.1029/2011JD016216, 2011.
- 975 Zhang, Z., Ackerman, A. S., Feingold, G., Platnick, S., Pincus, R. and Xue, H.: Effects of cloud
976 horizontal inhomogeneity and drizzle on remote sensing of cloud droplet effective radius: Case
977 studies based on large-eddy simulations, *J Geophys Res*, 117(D19), D19208–,
978 doi:10.1029/2012JD017655, 2012.
- 979 Zhang, Z., Werner, F., Cho, H. M., Wind, G., Platnick, S., Ackerman, A. S., Di Girolamo, L.,
980 Marshak, A. and Meyer, K.: A framework based on 2-D Taylor expansion for quantifying the
981 impacts of sub-pixel reflectance variance and covariance on cloud optical thickness and
982 effective radius retrievals based on the bi-spectral method, *Journal of Geophysical Research-*
983 *Atmospheres*, 2016JD024837, doi:10.1002/2016JD024837, 2016.
- 984